



UPPSALA
UNIVERSITET

*Digital Comprehensive Summaries of Uppsala Dissertations
from the Faculty of Science and Technology 2056*

Anti-Ageing Strategies

How to avoid failure in sodium-ion batteries

LE ANH MA



ACTA
UNIVERSITATIS
UPSALIENSIS
UPPSALA
2021

ISSN 1651-6214
ISBN 978-91-513-1252-1
URN urn:nbn:se:uu:diva-449511

Dissertation presented at Uppsala University to be publicly examined in Högssalen, Ångströmlaboratoriet, Lägerhyddsvägen 1, Uppsala, Friday, 24 September 2021 at 09:15 for the degree of Doctor of Philosophy. The examination will be conducted in English. Faculty examiner: Professor Philipp Adelhelm (Humboldt Universität zu Berlin).

Abstract

Ma, L. A. 2021. Anti-Ageing Strategies. How to avoid failure in sodium-ion batteries. *Digital Comprehensive Summaries of Uppsala Dissertations from the Faculty of Science and Technology* 2056. 56 pp. Uppsala: Acta Universitatis Upsaliensis. ISBN 978-91-513-1252-1.

In order to move away from fossil fuels, batteries are one of the most important technologies to store energy from renewable sources. The rapid demands of battery applications put pressure on supply chains of raw materials, such as lithium, nickel, copper, aluminium and cobalt. There is a concern about the availability of such elements in the future. Sodium-ion batteries based on naturally abundant elements have become an attractive alternative to lithium-ion batteries due to their potential to reduce the cost and to improve the sustainability of batteries. A low electrochemical cycling stability of these Na-ion batteries can hinder long-term implementation in large-scale applications. It is necessary to understand what can lead to ageing and electrochemical cycling failure in sodium-ion batteries and how such detrimental side-reactions can be prevented. Compared to lithium-ion batteries, the research on sodium-ion batteries is not as mature yet.

This thesis work sheds light on the ageing mechanisms at the electrode/electrolyte interfaces and in the bulk of electrode materials with the help of a variety of spectroscopic and electrochemical methods. The electrochemical properties at the anode/electrolyte interface have been carefully investigated with different galvanostatic cycling protocols and x-ray photoelectron spectroscopy (XPS). The solid electrolyte interphase (SEI) in sodium-ion batteries is known to be inferior to its Li-analogue and hence, its long-term stability needs to be thoroughly investigated in order to improve it. Fundamental properties of the SEI in regards to formation, growth and dissolution are investigated on platinum and carbon black electrodes in different electrolyte systems. As well as the use of unconventional additives have proven to saturate the electrolyte and to mitigate SEI dissolution. This work shows one of the few studies highlighting SEI dissolution using electrochemical cycling tests coupled with pauses, in order to detect SEI ageing in batteries. Ageing mechanisms in manganese-based cathodes have also been studied due to the abundance of manganese and their electrochemical performance at high voltages with synchrotron-based XPS, x-ray absorption spectroscopy (XAS), resonant inelastic x-ray scattering (RIXS) and muon spin relaxation measurements coupled with electrochemical techniques. Surface-sensitive studies revealed how capacity losses stem from electrolyte degradation which results in a redox gradient between surface and bulk electrode. The work also shows how anionic redox contributions and incomplete phase transitions are reasons of additional capacity losses observed in manganese-based cathodes. Furthermore, it shows how a low Na-mobility is also an indicator for inferior long-term cycling properties leading capacity losses.

Keywords: sodium-ion batteries, manganese-based cathodes, solid electrolyte interphase, ageing mechanism

Le Anh Ma, Department of Chemistry - Ångström, Structural Chemistry, Box 538, Uppsala University, SE-751 21 Uppsala, Sweden.

© Le Anh Ma 2021

ISSN 1651-6214

ISBN 978-91-513-1252-1

URN urn:nbn:se:uu:diva-449511 (<http://urn.kb.se/resolve?urn=urn:nbn:se:uu:diva-449511>)

*Dedicated to my parents, who gave
me the confidence and freedom to
pursue my goals.*

List of Papers

This thesis is based on the following papers, which are referred to in the text by their Roman numerals.

- I Ma, L.A., Naylor, A.J., Nyholm, L., Younesi, R. (2021) Strategies for Mitigating Dissolution of Solid Electrolyte Interphases in Sodium-Ion Batteries. *Angew. Chem. Int. Ed.* 60, 4855
- II Ma, L.A., Buckel, A., Nyholm, L., Younesi, R. (2021) Capacity losses due to solid electrolyte interphase formation and sodium diffusion in sodium-ion batteries. *Submitted manuscript.*
- III Ma, L.A., Massel, F., Naylor, A.J., Duda, L.C., Younesi, R. (2019) Understanding charge compensation mechanisms in $\text{Na}_{0.56}\text{Mg}_{0.04}\text{Ni}_{0.19}\text{Mn}_{0.70}\text{O}_2$. *Commun. Chem.* 2, 125
- IV Hakim, C., Sabi, N., Ma, L.A., Dahbi, M., Brandell, D., Edström, K., Duda, L.C., Saadoune, I., Younesi, R. (2020) Understanding the redox process upon electrochemical cycling of the P2- $\text{Na}_{0.78}\text{Co}_{1/2}\text{Mn}_{1/3}\text{Ni}_{1/6}\text{O}_2$ electrode material for sodium-ion batteries. *Commun. Chem.* 3, 9
- V Kim, E.J., Ma, L.A., Duda, L.C., Pickup, D.M., Chadwick, A. V., Younesi, R., Irvine, J.T.S., Armstrong, R. (2020) Oxygen Redox Activity through a Reductive Coupling Mechanism in the P3-Type Nickel-Doped Sodium Manganese Oxide. *ACS Appl. Energy Mater.* 3, 1, 184-191
- VI Kim, E.J., Ma, L.A., Pickup, D.M., Chadwick, A. V., Younesi, R., Maughan, P., Irvine, J.T.S., Armstrong, R. (2020) Vacancy-Enhanced Oxygen Redox Reversibility in P3-Type Magnesium-Doped Sodium Manganese Oxide $\text{Na}_{0.67}\text{Mg}_{0.2}\text{Mn}_{0.8}\text{O}_2$. *ACS Appl. Energy Mater.* 3, 11, 10423-10434

- VII Ma, L.A., Palm, R., Nocerino, E., Forslund, K.O., Matsubara, N., Cottrell, S., Yokoyama, K., Koda, A., Sugiyama, J., Sassa, Y., Månsson, M., Younesi, R. (2021) Na-mobility in P2-Na_{0.5}Mg_xNi_{0.17-x}Mn_{0.83}O₂ ($0 \leq x \leq 0.07$) from electrochemical and muon-spin relaxation studies. *Submitted manuscript*.

Disclaimer: Parts of this thesis are based on my licentiate thesis entitled *Cationic and anionic redox contributions in manganese-based cathode materials for sodium-ion batteries* (Uppsala University, 2020)

Reprints were made with permission from the respective publishers.

My contributions to the papers in this work

- I Planned most of the work, performed electrochemical, ICP-OES and XPS measurements. Wrote the manuscript with co-authors.
- II Planned most of the work, performed parts of electrochemical and XPS measurements. Wrote the manuscript with co-authors.
- III Planned most of the work, performed electrochemical, XRD and XPS measurements. Took part in the XAS and RIXS data analyses. Wrote the manuscript with co-authors.
- IV Performed XAS and RIXS measurements and took part in the overall discussion on the results.
- V Performed XAS and RIXS measurements and took part in the overall discussion on the results.
- VI Performed XPS measurements and took part in the overall discussion on the results.
- VII Planned most of the work, performed electrochemical measurements. Wrote the manuscript with co-authors. Took part in the discussion of the μ^+ SR results. Wrote the manuscript with co-authors.

Paper not included in the thesis

- Ma, L.A., Mogensen, R., Naylor, A.J. and Younesi, R. “Solid Electrolyte Interphase in Na-ion batteries” *Na-ion Batteries*, edited by L. Monconduit and L. Croguennec, WILEY, 2021. pp. 243-261.

Contents

1. Introduction.....	11
1.1 Importance of cycle life.....	11
1.2 Ageing processes at the anode/electrolyte interface.....	12
1.3 Ageing in manganese-based cathode materials.....	13
1.3.1 Structural stability.....	13
1.3.2 Reduction and oxidation processes.....	13
1.3.3 Na-diffusion.....	14
2. Scope of thesis	16
3. Methodology	17
3.1 Electrochemical testing	17
3.1.1 Galvanostatic cycling.....	17
3.1.2 Cyclic voltammetry	18
3.2 Spectroscopic characterization	19
3.2.1 X-ray photoelectron spectroscopy (XPS).....	19
3.2.2 X-ray absorption spectroscopy (XAS).....	21
3.2.3 Resonant inelastic X-ray scattering (RIXS).....	22
3.3 Muon spin relaxation technique	22
4. Results and discussion	24
4.1 Ageing mechanisms at the anode	24
4.1.1 Cycling protocols to determine capacity loss contributions	26
4.1.2 Elements affecting capacity loss at the anode	28
4.2 Ageing mechanisms at the cathode	33
4.2.1 Capacity losses in cathodes	33
4.2.2 Elements affecting capacity loss at the cathode.....	37
5. Conclusion and future work.....	44
6. Acknowledgements.....	47
7. Sammanfattning på svenska.....	48
8. References.....	50

Abbreviations

AP	After pause
BP	Before pause
CB	Carbon black
Ch	Charge
CV	Cyclic voltammetry
EC	Ethylene carbonate
DCh	Discharge
DEC	Diethylene carbonate
DFEC	Difluoroethylene carbonate
DME	1,2-dimethoxyethane
FEC	Fluoroethylene carbonate
FSI	Bis(fluorosulfonyl)imide
GITT	Galvanostatic intermittent titration technique
IMFP	Inelastic mean free path
IPFY	Inverse partial fluorescence yield
LIB	Lithium-ion battery
OCV	Open-circuit voltage
PC	Propylene carbonate
PFY	Partial fluorescence yield
RIXS	Resonant inelastic x-ray spectroscopy
SEI	Solid electrolyte interphase
SIB	Sodium-ion battery
SXAS	Soft X-ray absorption spectroscopy
TEY	Total electron yield
TFSI	Trifluoromethanesulfonimide
TFY	Total fluorescence yield
TM	Transition metal
VC	Vinylene carbonate
XANES	X-ray absorption near edge structure
XAS	X-ray absorption spectroscopy
XPS	X-ray photoelectron spectroscopy
XRD	X-ray diffraction

1. Introduction

1.1 Importance of cycle life

During the past decade, rechargeable lithium-ion batteries (LIBs) have become key components in electronic devices and in the electric vehicle industry due to their high energy and power density. However, due to the increasing use and demand of energy storage technologies, there are concerns regarding access to Li sources and to other elements used in LIBs (*i.e.* cobalt, nickel, and copper) [1]. In this respect, sodium-ion batteries (SIBs), in which only abundant elements can be used, are interesting alternatives due to their low cost and high sustainability. Especially for stationary energy storage, where the energy density is not as important, SIBs become attractive substitutes. Such stationary energy storage applications demand a sustainable and long-term electrochemical cycling performance. However, SIBs still suffer from degradation mechanism over usage time due to ageing. As a consequence, understanding the ageing processes and strategies to improve the cycle life are relevant for the researcher/developer community as well as the battery users [2–5]. Figure 1 illustrates a schematic of variety of ageing mechanisms which are most common in LIBs [5]. The ageing processes in SIBs are expected to be similar to those in LIBs in many aspects, but differences are also plausible.

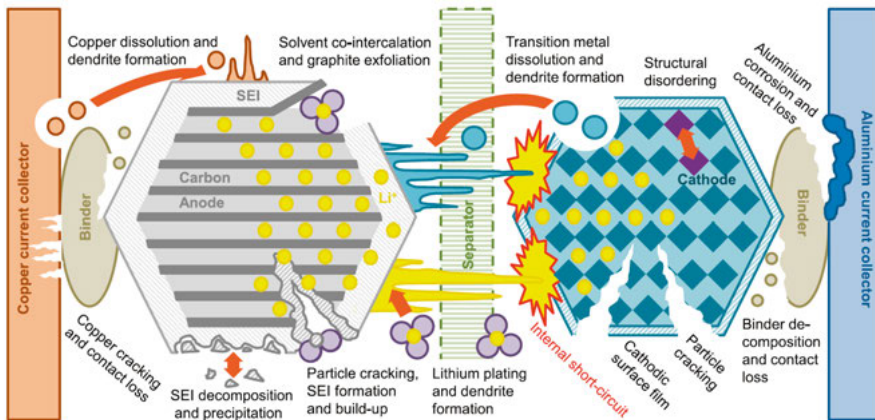


Figure 1. A schematic of different ageing mechanisms in LIBs [5]. Reprinted from reference 5 with permission from Elsevier. Copyright 1969.

1.2 Ageing processes at the anode/electrolyte interface

Degradation processes at the anode/electrolyte interface in Na-based systems are one of the major challenges in SIB development. Capacity losses due to such ageing events can either stem from the electrolyte, the anode/electrolyte interface and the anode itself.

In general, the electrolyte should have a high Na-ion conductivity to enable the lowest cell resistance possible, while being electrochemically stable against oxidation and reduction processes at the cathode and anode [6,7]. Due to the limited choice of electrolytes, most electrolytes are typically not stable at low potentials (< 1.0 V vs. Na^+/Na) and form a passivation layer on the surface of the anode which is called the solid electrolyte interphase (SEI). The composition of the SEI is mainly influenced by the electrolyte species since the SEI consists of electrolyte reduction products.

The concept of the SEI in an electrochemical system was first introduced by E. Peled in 1979 [8]. Peled proposed that an ideal SEI should be electronically insulating to prevent continuous electrolyte reduction and ionically conducting to allow Li- or Na-ions passing through to the anode. Lastly, the SEI should be chemically inert and insoluble. A continuous electrolyte reduction to form SEI should be prevented, because it consumes extra electrolyte and capacity, which limits the Na-inventory and severely shortens the battery cycle life [8–10]. Different electrolyte systems result in different SEI chemistry and stability. It is often stated that compared to its Li-counterpart, the SEI formed in Na-based systems is more soluble [11,12]. The dissolution of SEI species leads to continuous reformation of new SEI species, which is draining the capacity in a battery cell. Hence, in order to counterbalance the SEI dissolution, additives can be used. Conventional additives, such as fluoroethylene carbonate (FEC) or vinylene carbonate (VC) decompose before the actual electrolyte components and ensure the formation of a more stable and passivating SEI layer at the anode [11,13–15].

Most of the reported capacity losses in anodes are correlated to SEI formation and volume changes upon cycling. Volume changes can lead to SEI and particle cracking, and loss of electrical contact between current collector and active material [16]. A variety of studies also indicate diffusion-controlled ion trapping, meaning lithium or sodium trapped in the bulk electrodes. As a small fraction of the alkali-ions become inaccessible during cycling, the alkali-ion inventory is decreasing slightly, resulting in additional irreversible capacities [16–19].

A stable SEI at the anode is vital for the long-term performance of batteries. Capacity loss mechanisms at the anode/electrolyte interface are still not well understood, in particular the differences in chemical and electrochemical reactions between LIBs and SIBs governing the SEI properties. Hence, understanding the capacity losses stemming from the SEI and anode is crucial and can help to improve the battery cycle life.

1.3 Ageing in manganese-based cathode materials

For SIBs, many different types of electrode materials have been proposed which are similar to previous research approaches in LIBs [20–23]. Three main categories of cathode materials have been demonstrated for SIBs: layered oxides, polyanionic frameworks and Prussian blue analogues [20–23]. Among these three, the most extensively studied cathode type is the layered oxide of NaMO_2 -type (where M = metals, e.g. Mn, Ni, Co, Fe). The oxide layer consists of edge sharing M-O_6 octahedra sheets which are stacked on top of each other. Delmas et al. [24] established a nomenclature, which divides sodium-based layered oxides into two main categories depending on the sodium-ion position, at either octahedral (O-type) or prismatic (P-type) sites, with an attached number corresponding to the number of MO_2 per unit cell (Figure 2). The two major types of SIB cathode materials are either of P2 or O3 type. In P2 materials, the oxygen stacking sequence is ABBA, whereas in O3 it is ABCABC. Besides, there is also a P3-type structure which consists of oxygen stacking in the sequence ABCCA. Compared to P2-type materials, P3-type materials are considered to be more environmentally friendly due to their lower sintering temperature [25]. In this thesis, layered P2 and P3 Na_xMnO_2 derivatives are investigated. The layered manganese-based materials are attractive for SIBs due to their natural abundance, cost-effectiveness and high capacity [26,27].

1.3.1 Structural stability

Major challenges in such materials are the irreversible transitions of the P2 to the O2 phase at voltages above 4.0 V, which leads to structural degradation and hence a shorter lifetime [28–30]. One strategy to minimize the degradation at high voltages is to lower the cut-off potential. Moreover, P2- Na_xMnO_2 derivatives are also unstable in moisture. Due to the high spin Jahn-Teller effect of Mn^{3+} , water or carbonate molecules can be introduced into the structure [31]. Therefore, Ni ions can be inserted into P2- Na_xMnO_2 to obtain tetravalent Mn, as seen in P2- $\text{Na}_{2/3}\text{Ni}_{1/3}\text{Mn}_{2/3}\text{O}_2$. This material has an enhanced stability in moisture [32]. Generally, Ni-doped Na_xMnO_2 derivatives have gained increasing research attention because high capacities can be obtained due to the $\text{Ni}^{2+}/\text{Ni}^{4+}$ redox couple. Furthermore, a variety of dopants have been tested in Na_xMnO_2 cathode materials and showed an improvement in structural stability and overall electrochemical performance [29,33–36].

1.3.2 Reduction and oxidation processes

There is a large number of reports that discuss the redox activity of the incorporated transition metals (TMs) in Na-layered oxides. However, recent studies have also shown that not only cationic, but also anionic redox activities are

involved in charge compensation processes [37]. This indicates that the capacity can be stored both in TMs and oxygen ions [38]. Hence, the electronic nature of oxygen in such cathode materials is highly relevant for developing strategies to enhance the battery capacity. Oxygen redox activity (or in short: oxygen redox) is known to occur in Li- and Na-rich materials. Those alkali-metal rich compounds, however, suffer from oxygen loss during charging, leading to major reduction of cycle life [38,39]. Oxygen redox activities have also been observed in the cathode material $\text{Na}_{2/3}\text{Mg}_{0.28}\text{Mn}_{0.72}\text{O}_2$, indicating that no excess of Na is necessary to achieve oxygen redox. Additionally, unlike Na-rich compounds, $\text{Na}_{2/3}\text{Mg}_{0.28}\text{Mn}_{0.72}\text{O}_2$ does not undergo oxygen loss during cycling. This is due to the presence of Mg^{2+} , which suppresses the oxygen removal by interacting with O $2p$ orbitals in the structure [40]. Also, oxygen redox in the cathode material P2- $\text{Na}_{2/3}\text{Ni}_{1/3}\text{Mn}_{2/3}\text{O}_2$ has been reported [41]. The high capacity achieved was due to redox contributions of Ni, Mn and oxygen ions. However, in order to obtain such oxygen redox activities, high voltages need to be reached, which comes at the cost of oxidative electrolyte degradation, structural and electronic structure changes [26,30,42–44]. In summary, the importance of comprehensive studies on redox processes in battery cathodes is evident. The obtained information could help to spot ageing processes in cathode materials in SIBs and how to find the optimal balance between cycle life and extra capacity from redox mechanisms.

1.3.3 Na-diffusion

Even though octahedral (O3) cathodes hold more sodium per formula unit in ($x = 1$) than the prismatic (P2) structures ($0.6 < x < 0.7$), the Na-diffusion in O3 is slower than in P2, thereby affecting the electrochemical performance. The diffusion in O3 materials occurs via face-shared interstitial tetrahedral sites, whereas the Na ions in P2 structures travel through an open square consisting of oxide ions (Figure 2). Therefore, the diffusion barrier in P2 materials are expected to be lower than O3 materials, resulting in a better electrode performance [21,45]. It is important to understand such Na-ion diffusion pathways, in order to predict cycling performance and cycle life of a battery material.

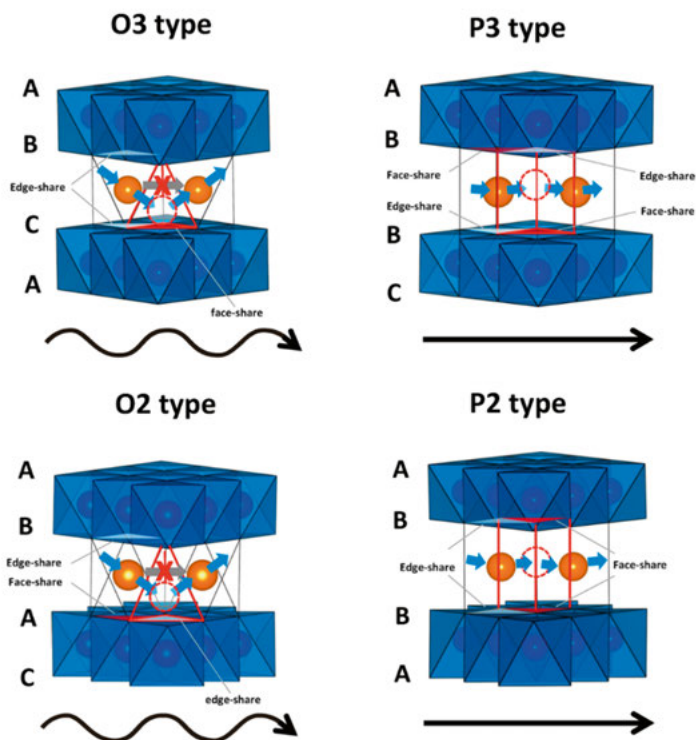


Figure 2. Different classification types of layered Na_xMO_2 compounds with edge-sharing M-O_6 octahedra sheets, displaying oxygen stacking sequences and corresponding Na-migration pathways [46]. Reprinted from reference 46 with permission from IOP Publishing. Copyright National Institute for Materials Science (NIMS). CC BY-NC-SA 3.0.

2. Scope of thesis

In this thesis, capacity losses due to ageing processes are studied with a variety of electrochemical measurements and synchrotron-based techniques. Using unconventional electrochemical tests and combinations of spectroscopy techniques has revealed a variety of ageing mechanisms. The thesis comprises seven papers discussing capacity losses observed in both the anode and the cathode. In the first part of the work, degradation processes at the anode/electrolyte interface, such as SEI dissolution and Na-loss mechanism are investigated. *Paper I* and *II* explore the capacity losses during pause at the anode/electrolyte interface in a variety of Na-based systems. *Paper I* focuses on the SEI dissolution and the effects of unconventional additives on metallic substrate, whereas *Paper II* discloses the capacity loss processes on carbonaceous electrodes and its influence on ageing mechanisms and the impact of such.

The second part of the work focuses on capacity losses observed in manganese-based cathode materials, including structural, redox and diffusion properties. In *Paper III-VII*, capacity loss mechanisms in different types of P2 and P3 manganese-based cathode material are studied. Besides structural changes at high voltages, other processes can add to capacity losses. With the use of XPS, XAS and RIXS, the aim is to identify capacity losses induced by oxygen redox and irreversible electronic rearrangements during cycling and to explore different redox activities in surface and bulk due to electrolyte degradation. In *Paper VII*, the Na-mobility in Mg-doped P2- $\text{Na}_{0.5}\text{Mg}_x\text{Ni}_{0.17-x}\text{Mn}_{0.83}\text{O}_2$ with different Mg-content is investigated with muon spin relaxation measurements and compared with its electrochemical performance. The muon spin relaxation results are in agreement with the electrochemical results and provide useful information regarding the Na-diffusion. The Na-mobility can limit the long-term cycling stability and result in higher capacity losses.

3. Methodology

3.1 Electrochemical testing

In order to investigate the ageing mechanisms in cells, galvanostatic and voltammetry tests were performed. In this work, the cell setup used is a two-electrode half-cell, which means that Na-metal as the counter electrode is also used as the reference electrode. Compared to a three-electrode cell, where counter and reference electrodes are separate units, two-electrode cells are less accurate. However, there is a lack of reliable reference electrodes for SIBs, and there also exist a complexity in building three-electrode cells, which together result in two-electrode cells being a practical option for battery testing. All mentioned potentials are measured in a half cell and hence, vs. Na^+/Na . In the discussion of cathodic and anodic materials tested in half cells, the terms discharge and charge are interchangeable with sodiation and desodiation, respectively. Using a half-cell setup provides unlimited source of Na-ions during cycling. However, the capacity fading discussed in this work focusses on the coulombic efficiency, hence the ratio between sodiation/desodiation capacity. In a full-cell, such capacity losses can result in depletion of Na-inventory, assuming that at least one of the electrodes is capacity limiting.

3.1.1 Galvanostatic cycling

Galvanostatic testing is the most common technique to mimic the performance in battery applications. During galvanostatic testing, a constant current is applied while the potential is recorded until a cut-off value is reached, and then the current is reversed to reach the other cut-off potential. The cut-off potential defines the potential range of the test. For this, a galvanostat is needed and it supplies and measures the current between working and counter electrode.

Cycling conditions in this thesis are either given in C-rate or current density. A C-rate of 0.1 (or 1/10) C corresponds to 10 h charge or discharge. The capacity Q is presented in the unit “mAh/g” instead of SI units for charge (Coulomb, C) to possibly avoid confusion between the C-rate and the capacity. Current densities describe either the amount of current per cross-sectional area of the electrode or per active material mass and are given here in “ $\mu\text{A}/\text{cm}^2$ ” or “mA/g”, respectively.

One can also plot the potential V against the capacity Q or the capacity Q versus the cycle number. An additional analysis method is plotting the differential capacity (dQ/dV) as a function of the potential based on the galvanostatic results. The advantage of the dQ/dV analysis is that the plateaus seen in the potential-capacity plots can be identified as peaks [47,48].

In this work, a variety of cycling protocols have been used in order to determine capacity losses. For this, the cells are cycled five times before a pause at open-circuit voltage (OCV) for a specific number of hours. A subsequent sodiation or desodiation cycle is implemented after the pause. The determined capacity can provide information on the magnitude of capacity loss observed during pause. Details are discussed in *Paper II*. Such combinations of cycling and pauses at OCV are inspired by Dahn et al. [14], whom studied the growth of the SEI and the capacity loss after a pause of 550 h in Li/graphite cells.

In addition to constant current cycling, galvanostatic intermittent titration technique (GITT) is used to determine the Na-ion diffusion coefficient upon cycling. For this, a series of current pulses followed by relaxation via current interruption is applied until reaching the cut-off potential. The chemical diffusion coefficient of Na-ions D_{Na^+} can then be calculated from the following equation [49–51]:

$$D_{Na^+} = \frac{4}{\pi} \left(\frac{i V_m}{z_A F S} \right)^2 \left(\frac{dE/d\delta}{dE/d\sqrt{t}} \right)^2 \quad (\text{Eq. 1})$$

where i is the pulse current, V_m the molar volume, z_A the charge number (1 for Na^+/Na), F the Faraday constant, S the electrode surface area, $dE/d\delta$ the steady state voltage changes after each titration step δ , $dE/d\sqrt{t}$ the voltage changes during a current pulse in relation to the pulse time \sqrt{t} .

3.1.2 Cyclic voltammetry

For cyclic voltammetry a potentiostat is required, which records the current generated at an applied potential, and can give information on redox activities or other reactions of the material at certain voltages. Reversible reactions result in two peaks, an oxidation and a reduction peak, whereas for irreversible reactions, only one peak will appear. The peaks can be distinguished between oxidation and reduction by the direction of the current. The potential can be swept at different rates, which is called the scan rate. At low scan rates, reactions with low rate constant can be observed. In this work, the technique has been used to identify transition metal redox activities and phase transitions in a given potential range [47].

3.2 Spectroscopic characterization

3.2.1 X-ray photoelectron spectroscopy (XPS)

Surface analysis was performed with XPS, which is an important technique to probe thin surface layers. In XPS analysis, samples are irradiated by X-rays and the kinetic energy of emitted photoelectrons (Figure 3, XPS), based on the photoelectric effect, is measured with a hemispherical analyzer [52].

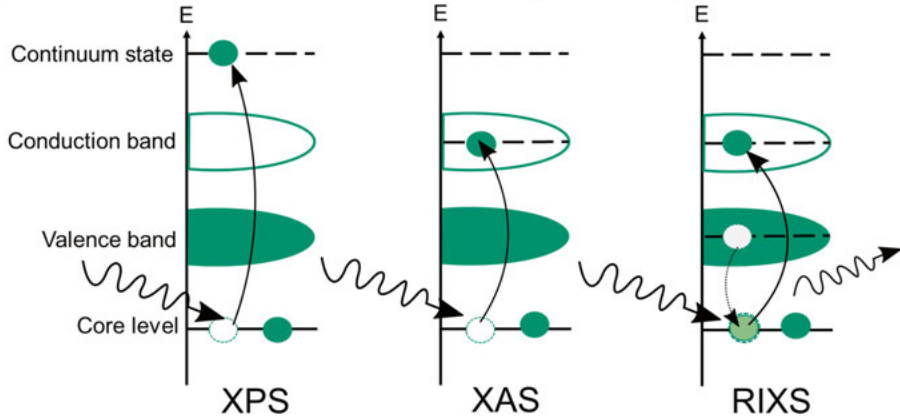


Figure 3. Scheme of spectroscopic processes in XPS, XAS and RIXS.

The distance an electron can travel is limited and depends on the inelastic mean free path (IMFP), which makes the technique highly surface sensitive. The probing depth is in nanometers range. The kinetic energy of the emitted electron depends on two factors: how strongly it was bound and the energy of the incident photon from the X-ray, and is defined as following:

$$E_{Kin} = h\nu - E_B - \Phi_s \quad (\text{Eq. 2})$$

In equation (Eq. 2), E_{Kin} is the measured kinetic energy of the electron, $h\nu$ is the energy of the incoming photon, E_B is the binding energy of the orbital where the electron is removed from and Φ_s is the work function which is specific for every spectrometer. The binding energy E_B is specific for every element and depends on the chemical state, which enables precise identification and quantification of elements in a material.

In synchrotron facilities, it is possible to have energy-tuned X-rays and hence the energy of the incoming X-ray hitting the sample can be gradually changed to provide information at different depths. The higher the energy of the irradiating X-ray, the higher the kinetic energy of the emitted electron (see equation Eq. 2).

One should be careful with the analysis of XPS data, because XPS spectra can include Auger peaks which can be identified as false peaks, or the sample can be charged during the measurement, which causes a peak shift. In this

work, all XPS spectra are calibrated with an internal standard, which is the hydrocarbon peak at 285 eV. With internal standards, the work function and sample charging can be disregarded, if the sample charging is considered to be constant.

3.2.1.1 Normalization and elemental quantification

Elemental quantification on the surface composition can be determined with the help of the core level peak intensities. Besides the elemental concentration, the intensities depend on the probability of photoelectron emission from that probed core level (the cross section σ) and the aforementioned inelastic mean free path (λ). In this thesis, the Scofield cross section [53] and the IMFP values for polyethylene [54] were used. The relative intensity of a core level peak can be obtained by normalizing the peak area with the cross section and the IMFP divided by the sum of normalized peak areas of all the elements in that sample [55].

3.2.1.2 Depth profile analysis

In this thesis, the probing depth corresponds to three times the IMFP value for polyethylene, stemming from the observations that 95% of all emitted photoelectrons are from a depths of 3λ [56]. For example, in *Paper III*, the synchrotron-based beamline I09 at the Diamond Light Source (Oxfordshire, UK) was used. XPS spectra have been recorded using photon energies of 1090, 2350 and 7050 eV (Figure 4, XPS), which correspond to probing depths of 10 nm, 17 nm and 50 nm.

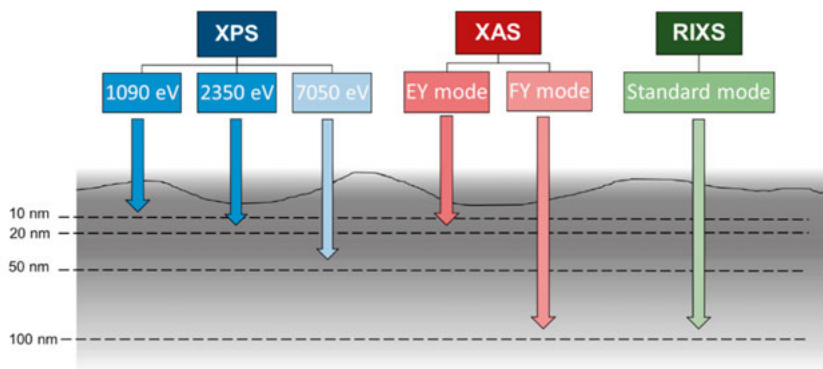


Figure 4. Depths of analysis for XPS, XAS and RIXS techniques in this work.

3.2.2 X-ray absorption spectroscopy (XAS)

The XAS technique uses a wide range of tunable X-rays provided by synchrotron facilities to identify the oxidation state of ions in different samples. Incident photon energies irradiating the samples are scanned across an absorption edge creating a core hole state (Figure 3, XAS). The area underneath an absorption spectrum represents the partial density of unoccupied states above the Fermi level. The spectra can be separated into three different regions: the pre-edge region describes core electron excitation to unoccupied states close to the Fermi level, the main-edge probes the upper quasi-bound states, and the post-edge which leads to excitation above the ionization threshold [57–59].

The response to each incident photon energy can be detected as either transmitted X-rays, fluorescence or electron yield. There are direct and indirect detection modes. Transmission mode is a direct detection mode, which identifies first-order absorption processes. Due to the short attenuation lengths of soft x-rays, XAS measurements in transmission mode are only relevant for thin samples, and not for common battery materials. Hence, indirect detection modes are more suitable for battery analysis and rely on secondary processes which are separated into radiative and non-radiative relaxation. In the latter case, the generated core hole state relaxes back to the ground state by filling the core-hole with an electron from a higher energy level via the emission of an Auger electron. The Auger electron can then scatter inelastically and create low energy secondary electrons which leave the sample. The generated number of core holes is proportional to the drain current to replace the lost photoelectrons, which is measured by a high precision ammeter. This detection mode is surface sensitive, with probing depths of 2-10 nm (Figure 4, XAS), due to the short attenuation length of the scattered electrons and is called the total electron yield (TEY). Another mode of indirect detection is total fluorescence yield (TFY). The excited system relaxes back to ground state by filling the core hole with a valence level electron via emission of a photon with the energy difference of the two energy levels. The TFY detection is more bulk sensitive (up to 100 nm), because photons have a longer attenuation length than electrons. In TFY mode, photons are detected with a photodiode or a Channeltron. If an energy resolved detector is used, which limits the sensitivity to a certain emission energy range, the detection mode is called partial fluorescence yield (PFY) [57,58,60,61]. For thick samples, a method which is free from artifacts such as self-absorption effects, is called inverse partial fluorescence yield (IPFY). This is based on the fact that the fluorescence of a lower-energy transition decreases inversely proportional to the excitation of the resonant edge. For the IPFY approach, a spectator element with a lower-energy absorption edge than the element of interest is required. In this work, the IPFY method is shown on the Mn L-edge using the O K-edge.

Two additional terms in XAS are used: soft X-ray absorption spectroscopy (SXAS) and X-ray absorption near edge structure (XANES). SXAS describes

the use of X-rays with an upper energy limit of 5 keV. XANES describes the technique of probing excitations from core levels into unoccupied energy states [62].

3.2.3 Resonant inelastic X-ray scattering (RIXS)

RIXS is a complementary, bulk-sensitive measurement to XAS, where instead of unoccupied states, the density of occupied states and charge neutral excitations are probed (Figure 3, RIXS). RIXS measurements consist of two processes (Figure 3, RIXS): the resonant absorption of the incident photon with known energy and the emission of another photon with different energy. The difference in energies can lead to varying excitations in the system. In RIXS measurements, photons are inelastically scattered and may generate localized excitations which are reflected by spectral signatures with specific energy loss and momentum loss. Information on the excitation can be deduced from the measured change in energy and momentum of the scattered photon and the dependence on the incident polarization. Particularly, the incident energy dependence of RIXS has the power to reveal different species of the same element, such as localized versus band-like oxygen states. In XAS, the incident photon energy is tuned to a certain absorption edge to probe elemental and orbital nature. Using the exact energy of a certain absorption can highlight specific transitions to observe more well-defined chemical bonds or oxidation states of different atomic species. Compared to XAS, where photons are summed up to one intensity data point, the emitted photons in RIXS measurements are separated by their different emission energies. Furthermore, unlike in XAS where incident photon energies are scanned, one incident photon energy is held for longer time in RIXS measurements to enable good statistics of the emission energies. Sweeping a range of photon energies is also possible and results in a RIXS map. By integrating the RIXS map, one would obtain a PFY-mode XAS spectrum [63].

3.3 Muon spin relaxation technique

The muon spin relaxation (μ^+ SR) technique is a powerful method to study condensed matter physics of a material [64–66]. In general, the μ^+ spin relaxation is used to study electron physics, such as magnetism [67–71] and superconductivity [72,73]. Recently, the scope of this technique has broadened notably and are now also used to investigate charge dynamics in Li/Na/K-ion batteries [64,74–80].

In the context of this thesis work, muons are used to determine the Na-ion diffusion determined by parameters such as activation energy E_a , Arrhenius factor A and hopping rate at different temperatures. Based on these values, the rate constant is determined from the Arrhenius equation [81,82]:

$$k = A \times e^{-\frac{E_a}{RT}} \quad (\text{Eq. 3})$$

where k is the rate constant; its unit is dependent on overall reaction order, which is here assumed to be a first order reaction $\left[\frac{1}{s}\right]$. A is Arrhenius factor or pre-exponential factor and E_a the activation energy, R the ideal gas constant and T the temperature.

4. Results and discussion

4.1 Ageing mechanisms at the anode

This chapter discusses the capacity losses observed at the anode/electrolyte interface with regards on the solid electrolyte interphase (SEI) and is based on *Paper I* and *II*.

Possible mechanisms that lead to capacity losses on the anode side include SEI formation, SEI dissolution, loss of active materials, ion-trapping, etc. One of the major drawbacks in SIBs compared to its Li-counterpart is the inferior SEI stability in Na-based systems [11,12]. Therefore, it is essential to have a more fundamental knowledge about SEI dissolution and other capacity loss mechanisms in Na-based electrolytes, in order to improve its long-term stability. In *Paper I* and *II*, capacity losses in Na-based systems were studied thoroughly with a special cell setup using either platinum (Pt) foil or carbon black (CB) as the working electrode, Na-metal as the counter electrode, non-aqueous liquid electrolytes and Na-conductive β -alumina as separators, as shown in Figure 5a. The study on the platinum substrate (*Paper I*) helps to focus solely on SEI dissolution and to exclude other capacity loss processes such as Na-trapping and volume expansion resulting in electrode cracking. On the other hand, the study with CB electrodes (in *Paper II*) leads us to understand the capacity losses in carbonaceous electrodes, which does not only involve SEI dissolution as in *Paper I*, but also includes influences from Na insertion/extraction upon cycling. In all these studies, the cell voltage always remained above 0 V vs. Na^+/Na to avoid alloying and underpotential deposition of Na. The use of Na-conductive β -alumina separators can minimize crosstalk stemming from the electrolyte decomposition products formed in contact with the metallic Na-electrode and diffusing to the working electrode, affecting the electrochemistry and SEI stability as seen in Figure 5b [83]. Electrochemical tests in *Paper I* and *II* have shown that lower capacity losses are observed without Na-conductive β -alumina separators, which can be due to the absence of the decomposition products from the Na-metal electrode. Such electrolyte decomposition products can be similar to the SEI compounds, which would saturate the electrolyte with potential SEI components and hence decrease the SEI dissolution. However, in order to gain a fundamental understanding on SEI stability and to compare different systems, such crosstalk needs to be prevented. Figure 5c shows an example of one galvanostatic cycling protocol

from *Paper II* and how the capacity loss values are obtained. The cycling protocol with implemented open-circuit pauses at a low potential enabled us to examine the self-discharge during pause. As seen in Figure 5c, there is a potential increase over the pause time indicating self-discharge due to the instability of SEI. In this example, the capacity loss after an open-circuit pause is based on the reduction capacity (self-discharge cycle) measured after the pause. The capacity losses, plotted as a function of the square root of the pause times, demonstrate a linear correlation, which implies capacity loss due to diffusion-controlled processes.

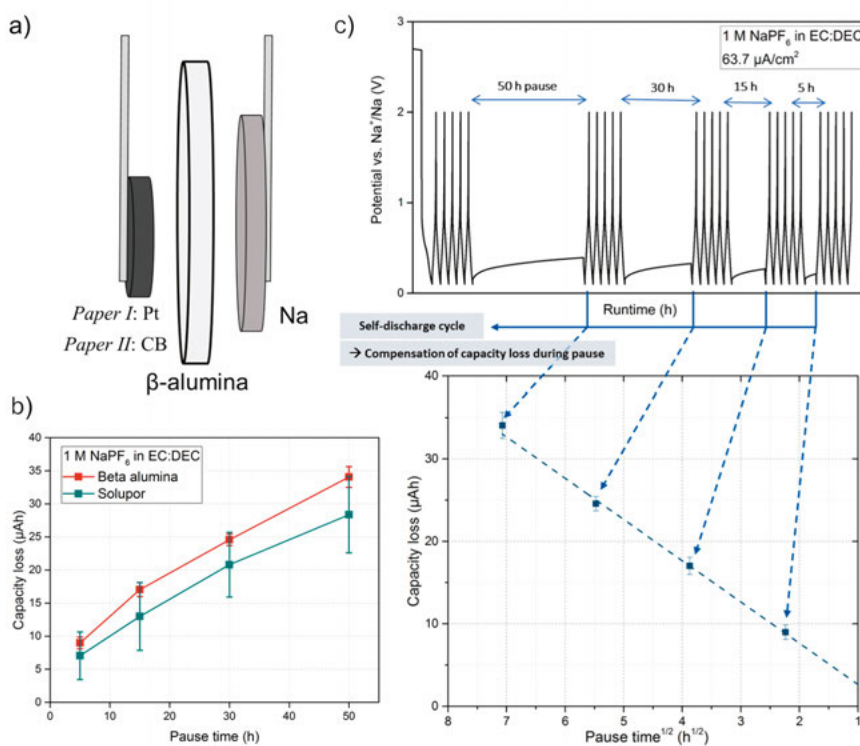


Figure 5. Experimental setup to determine anodic capacity loss. The shown error bars are based on the standard deviation of three replicate cells. a) Schematic cell setup used in Paper I and II. b) Absolute capacity loss with Solupor® separator in comparison to Na-conductive β -alumina from Paper II. A lower capacity loss with Solupor® separators could stem from species formed at the Na-metal, which saturates the electrolyte and hence prevent additional SEI dissolution. Using β -alumina reduces the crosstalk effects and enables studying the electrolyte system without the influences of species formed at the Na-metal. c) Cycling protocol and the capacity losses after each pause as a function of the square root of the pause times, from Paper II. The linear correlation suggests that the observed capacity losses are due to diffusion-controlled processes.

4.1.1 Cycling protocols to determine capacity loss contributions

In this thesis, capacity losses are investigated via galvanostatic cycling experiments with subsequent pauses at open-circuit voltage (OCV), inspired by the work of Sinha et al. [14]. At low electrode potential, the electrolyte becomes reduced and forms a passivation layer, the SEI. The reduction capacity measured in the first cycle is significantly larger than in the following cycles, which indicates SEI formation. After cycling five times between 0.2 mV to 2.0 V (for Pt electrodes) or in the range 0.1–2.0 V (for CB electrodes), the cell is stopped for 50 h, 30 h, 15 h and 5 h without any applied current, before the cycling is continued for five times again.

Figure 6 shows the three different cycling protocols used to investigate capacity losses in CB electrodes during pause due to different ageing mechanisms. In Protocol 1 (Figure 6a), the cell was stopped for 50 h at 0.1 V, followed by discharge back to 0.1 V, which led to a potential increase over time. After pause, the cell was once again discharged (repeated sodiation of carbon black) down to 0.1 V. The measured discharge capacity (DCh-AP) should correspond to a “refill” of lost Na^+ during the pause (Figure 6b) which can be due to following processes: i) during pause, the SEI dissolves partially back into the electrolyte and the reduced carbon, meaning Na^+ and e^- in the CB at 0.1 V, reacts with the electrolyte to counterbalance SEI dissolution and/or ii) Na, both Na^+ and e^- , diffuse further into the bulk electrode with time (Na-trapping), which can lead to a Na^+ concentration depletion at the surface of the CB electrode, making room for more Na^+ to be inserted during the next reduction cycle after pause. In lithium-based batteries, such ion-trapping phenomena have also been reported before [18,19,84].

For protocol 2 (Figure 6a), the CB electrode was, same as above, stopped at 0.1 V for 50 h, but this time a charge cycle was implemented after the pause (desodiation of CB). In contrast to the first protocol, where a sodiation cycle followed after the pause, protocol 2 enables to determine the rest of Na, which can be reversibly extracted from the CB structure. By taking the difference between the charge capacity after pause (Ch-AP) and before pause (Ch-BP), the capacity loss due to Na-loss (from reaction of reduced carbon and Na-trapping) can be determined (Figure 6b). Hence, protocol 1 and 2 should measure the same process –the Na-loss during pause.

With protocol 3 (Figure 6a), the cells were paused at high potential of 2.0 V and then sodiated (discharged). The discharge capacity after the pause (DCh-AP) corresponds to rebuilding the SEI in case of SEI dissolution during the pause and the general Na^+ re-insertion into the CB structure at every sodiation cycle. Under the assumption of consistent Na-insertion after the second cycle, the difference between the discharge capacity before pause (DCh-BP) and after pause (DCh-AP) can cancel out the contribution of sodiation per cycle. In the end, the capacity loss can be related to mostly SEI dissolution (Figure 6b).

In contrary to protocol 1 and 2, the Na-trapping effect of intercalated Na in the CB electrode is negligible.

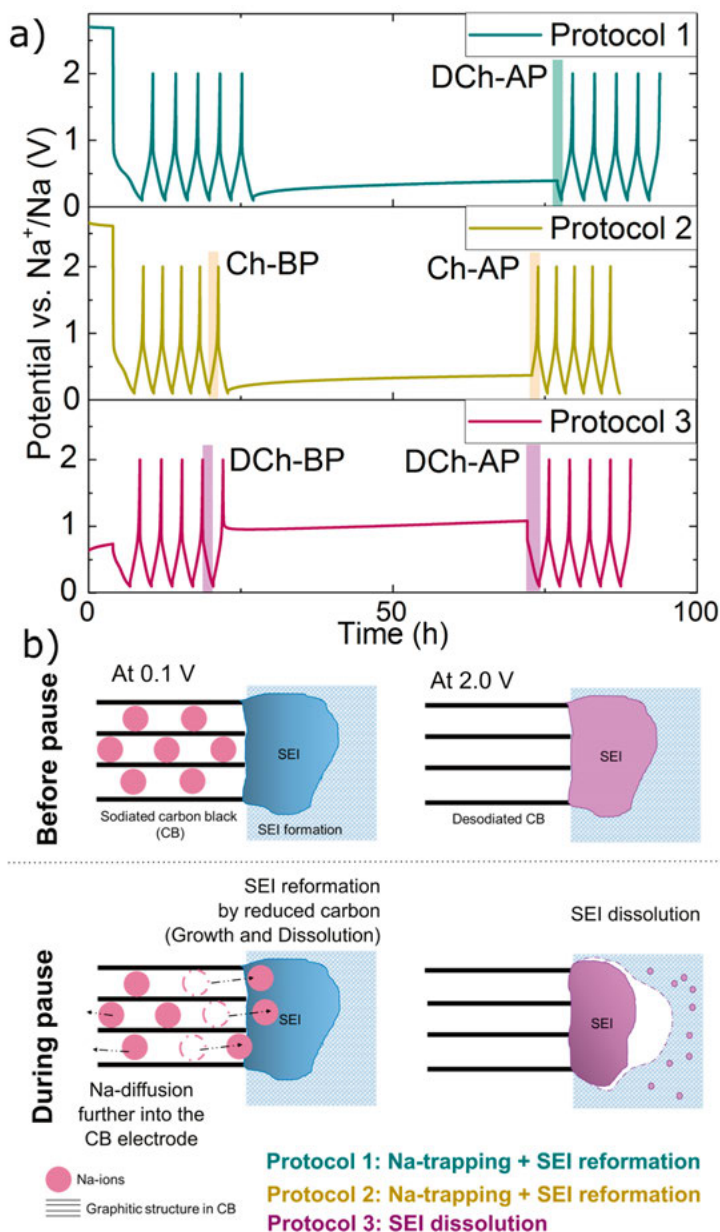


Figure 6. Capacity losses observed in carbon black electrodes from Paper II. a) Cycling protocols shown as potential vs. time to determine capacity loss contributions in CB electrodes. Cells were cycled five times between 0.1 and 2.0 V with a current density of $63.7 \mu\text{A}/\text{cm}^2$, and then stopped at a specific potential, followed by a pause of 50 hours with no external potential or current applied. b) Schematic illustration of ageing mechanisms identified with the three cycling protocols from a).

Table 2 shows the capacity losses from the three aforementioned cycling protocols in two different Na-based electrolyte systems: 1 M sodium hexafluorophosphate (NaPF₆) and 1 M sodium trifluoromethanesulfonimide (NaTFSI) in ethylene carbonate (EC): diethylene carbonate (DEC) (vol, 1:1) with a pooled standard deviation. As discussed in detail in *Paper II*, the largest capacity losses for both electrolyte systems are observed in protocol 1 (followed by protocol 2), because capacity losses due to SEI dissolution and Na-trapping are taken into account. Protocol 2 should measure the same contributions of Na-loss as in protocol 1. According to Table 2 along with the pooled standard deviation values, the measured capacity loss due to Na-loss is similar in both electrolytes. On the other hand, the difference between protocol 1 and 2 is insignificant in perspective of the pooled standard deviation (6 groups with 3 replicates each), assuming the variance in all groups is the same. Protocol 3 illustrates the capacity losses due to mostly SEI dissolution, which is also similar in both electrolyte systems. However, one needs to be aware that protocol 3 stopped at a high potential of 2.0 V, which could cause deviations in the SEI surface chemistry, leading to a different SEI stability.

Thus, in order to determine the capacity losses incorporating both Na-loss and SEI change, cycling protocol 1 should be used when studying ageing mechanism on CB (*Paper I*). Due to the absence of Na-loss on Pt electrodes, protocol 3 was used for SEI dissolution studies on Pt-substrates (*Paper I*).

Table 2. Capacity losses obtained after a 50-hour pause at open-circuit in 1M NaPF₆ in EC:DEC and 1M NaTFSI in EC:DEC from the galvanostatic protocols shown in Figure 6a from Paper II. The pooled standard deviations are based on data from three replicate cells.

Cycling Protocols	Capacity loss types	1 M NaPF ₆ -EC:DEC	1 M NaTFSI-EC:DEC
1	Na-trapping and SEI reformation	34 ± 3.3 μAh	28 ± 3.3 μAh
2	Na-trapping and SEI reformation	23 ± 3.3 μAh	24 ± 3.3 μAh
3	SEI dissolution	8 ± 3.3 μAh	9 μ ± 3.3 μAh

4.1.2 Elements affecting capacity loss at the anode

This chapter discusses the factors determining the magnitude of capacity losses after a pause.

4.1.2.1 Electrolyte volume

Paper I and *II* have shown that the measured capacity loss after pause is dependent on the electrolyte volume. For example, with CB electrodes in 1 M NaPF₆-EC:DEC (Figure 7), the capacity loss after 50 h pause increases by

27% when doubling the used electrolyte volume from 150 μl to 300 μl . Interestingly, by extrapolating the linear fit to the y-axis, the capacity loss at zero electrolyte volume is 25 μAh , which is similar to the capacity loss obtained with protocol 2. At zero electrolyte volume, the capacity loss should mostly be influenced by Na-trapping contributions, whereas with increasing electrolyte volume, the additional capacity losses could be a result of SEI dissolution. Thus, the electrolyte volume can minimize the amount of capacity loss stemming from SEI dissolution.

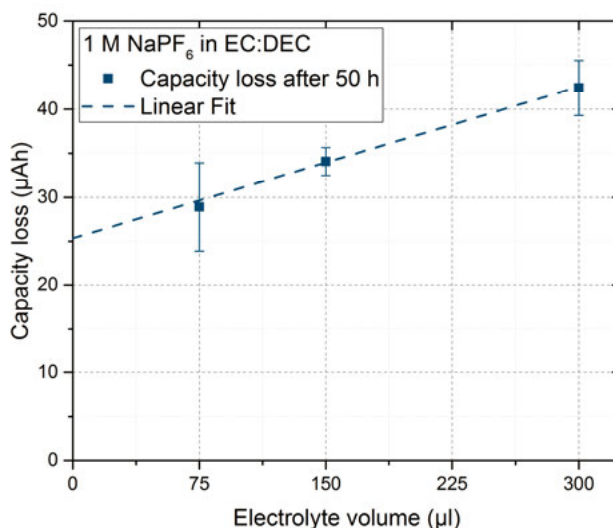


Figure 7. Capacity loss after 50 h depending on the electrolyte volume, with a linear fit with 1 M NaPF₆-EC:DEC electrolyte from Paper II. The error bars show the standard deviation of three replicate cells.

4.1.2.2 Electrolyte salt and solvent

The choice of electrolyte salt and solvent also plays an important role in ageing. According to the electrochemical results for the tested electrolyte matrix in Paper II (see Figure 8), the solvent mixture EC:DEC resulted in the highest capacity loss for three different electrolyte salts, *i.e.* NaPF₆, sodium bis(fluorosulfonyl)imide (NaFSI) and NaTFSI. However, with the solvent mixture EC:1,2-dimethoxyethane (DME), significantly lower capacity losses are observed with the same salts. Amongst the electrolyte salts, NaPF₆ showed in average the highest capacity losses and with NaTFSI salt, less capacity losses after pause are observed.

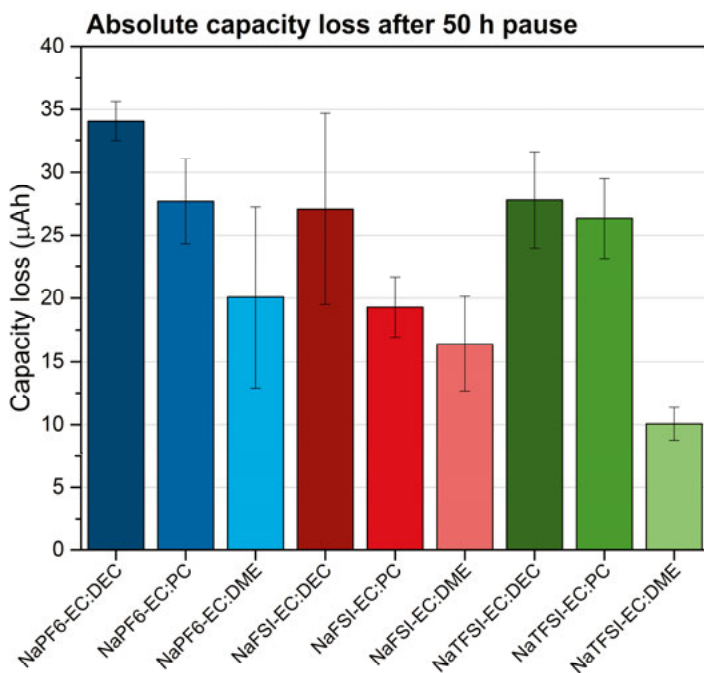


Figure 8. Absolute capacity loss after 50 h pause in nine different electrolyte systems from Paper II. The lowest capacity loss is observed for 1 M NaTFSI-EC:DME, whereas the highest is for 1 M NaPF₆-EC:DEC. The error bars indicate the standard deviation of three replicate cells.

Another major source of capacity loss can occur during cycling. Due to unstable SEI formation/growth, the electrolyte becomes continuously reduced to rebuild the SEI, which consumes more capacity and could lead to electrolyte depletion over time. The magnitude of the irreversible capacity in the initial cycles, which as in Paper II for CB electrodes is defined as the difference between reduction and oxidation capacity, can therefore give information on the long-term stability of the SEI and electrolyte. Figure 9 shows the accumulated irreversible capacities in nine different electrolyte systems from cycle 1-5. The capacities are furthermore distinguished between a formation capacity (Figure 9, cycle 1) and a growth capacity (Figure 9, cycle 2-5). The highest irreversible capacity for cycle 1-5 is observed for NaPF₆-EC:DEC, whereas the lowest appear in NaPF₆-EC:DME and NaTFSI-EC:DME. With respect to the growth capacities in cycle 2-5, more capacity is required in NaPF₆-EC:DEC (ca. 40 μAh) compared to NaTFSI-EC:DME (ca. 10 μAh), suggesting that the SEI in NaPF₆-EC:DEC is not sufficiently stable, which leads to continuous electrolyte reduction during the following cycles.

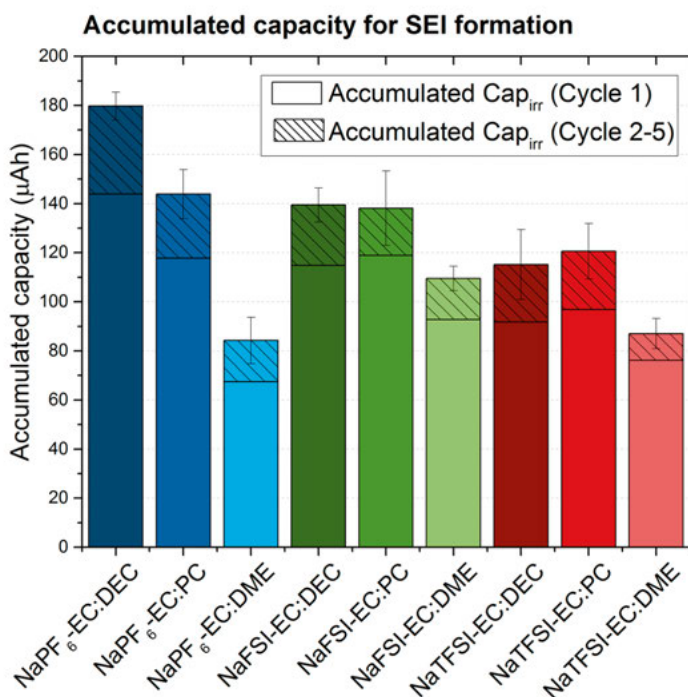


Figure 9. Galvanostatic results for nine different electrolytes systems from Paper II. The error bars illustrate the standard deviation of three replicate cells. Accumulated irreversible capacities for cycles 1-5 correspond to the charge consumed for SEI formation/growth. Irreversible capacity is defined as the difference between reduction and oxidation capacity. The accumulated irreversible capacities are separated into formation capacity (cycle 1) and growth capacity (cycle 2-5). The SEI formed in NaPF₆-EC:DEC consumed the most capacity (180 μAh), whereas NaPF₆-EC:DME and NaTFSI-EC:DME consumed only 80 μAh each.

In addition, the electrolyte salt can also influence the ageing mechanisms. Figure 10 displays bulk sensitive $C 1s$ spectra of CB samples in 1 M NaPF₆ and 1 M NaTFSI in EC:DEC and EC:DME solvent systems and of the pristine CB. The peak at 284.0 eV represents the pristine electrode. Hence, an increase or decrease of this peak after a pause indicates either SEI dissolution or growth, respectively. With NaPF₆, a thicker SEI is observed after pausing, while especially in EC:DEC the SEI becomes significantly thicker compared to EC:DME. When using NaTFSI salt in the same solvents, a different SEI behaviour is observed. In combination with EC:DEC, the SEI dissolves notably, but with EC:DME only slightly. Consequently, the choice of electrolyte salt can define the ageing mechanisms, whereas the choice of solvent mixtures substantially influences the magnitude of capacity loss due to ageing types, such as SEI dissolution and growth after pause.

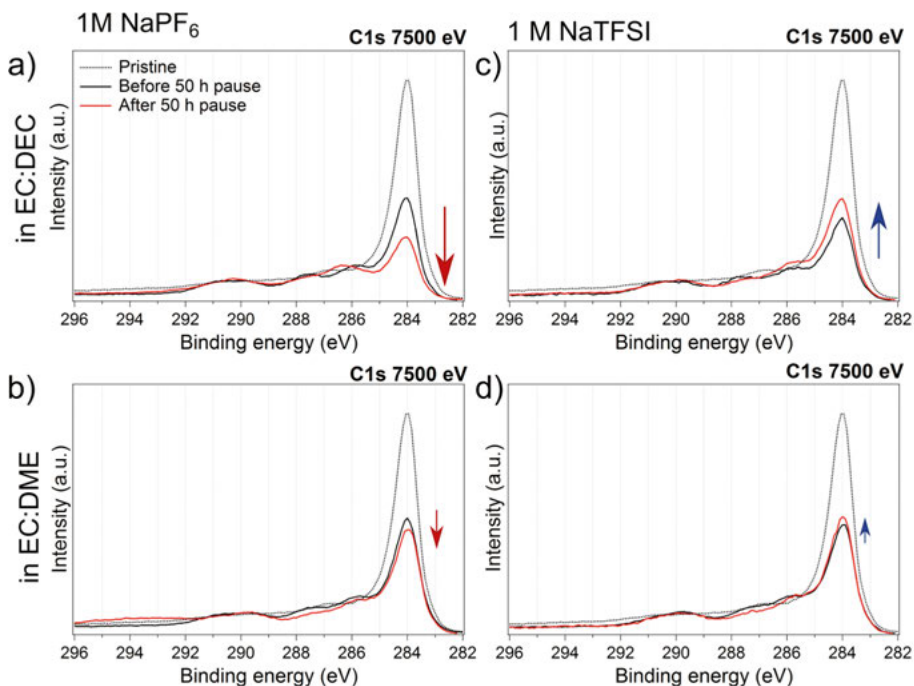


Figure 10. SEI growth after a 50-hour pause in $\text{NaPF}_6\text{-EC:DEC}$ and -EC:DME indicated by decrease of the pristine CB peak at 284.0 eV and SEI dissolution after pause, suggested by a slight peak increase in NaTFSI-EC:DEC and -EC:DME . Bulk sensitive C1s spectra a) in $\text{NaPF}_6\text{-EC:DEC}$ and b) in $\text{NaPF}_6\text{-EC:DME}$ with a peak decrease (red arrow), and c) in NaTFSI-EC:DEC and d) NaTFSI-EC:DME with peak increase (blue arrow).

4.1.2.3 Additives

Another method to minimize such capacity loss is to tackle the degree of SEI dissolution with electrolyte additives. Conventional additives such as fluoroethylene carbonate (FEC), difluoroethylene carbonate (DFEC) and vinylene carbonate (VC) focus on the formation of a stable SEI on the anode surface [11,13]. Another approach would be the use of soluble SEI components such as NaF and Na_2CO_3 as additives (Figure 11) to shift the SEI dissolution equilibrium, which is highlighted in *Paper I*. Particularly, the addition of NaF and Na_2CO_3 in 1 M NaPF_6 in PC helped decreasing the capacity loss rate (Figure 11a). One reason why the capacity loss could be successfully decreased in $\text{NaPF}_6\text{-PC}$ is that the added species, such as NaF, could be incorporated into the SEI during cycling as shown in Figure 11b, to establish a more stable inorganic SEI character resulting in less capacity loss. Clearly, there are other SEI species which can go into dissolution during the pause, besides NaF and Na_2CO_3 , but this could be the first step towards more unconventional additive strategies to decrease SEI dissolution.

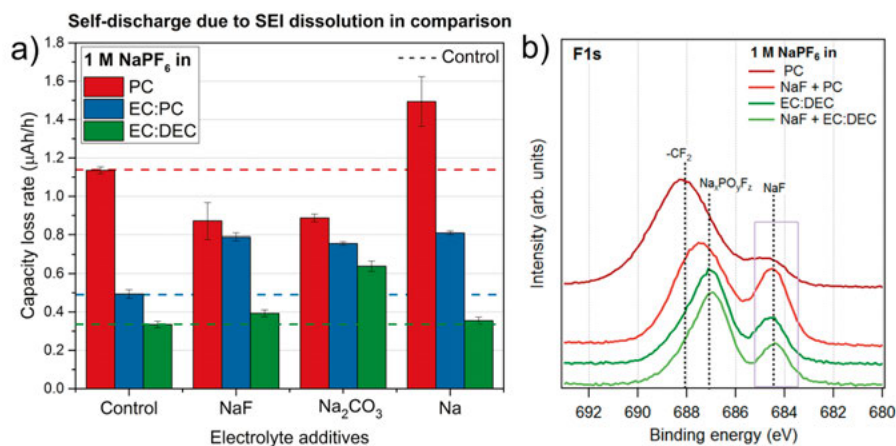


Figure 11. Influence of NaF, Na_2CO_3 or Na-metal addition in 1 M NaPF_6 in PC, EC:PC and EC:DEC from Paper I. a) Capacity loss rates obtained from electrochemical results from protocol 3 prior (control) and after additives. b) F 1s spectra illustrating the influence of NaF addition in 1 M NaPF_6 in PC and EC:DEC. No significant effect is seen for 1 M NaPF_6 in EC:DEC, whereas in PC NaF is incorporated in the SEI after NaF addition.

4.2 Ageing mechanisms at the cathode

This chapter sheds light on the capacity fading in different manganese-based cathode materials, such as $\text{P2-Na}_{0.56}\text{Mg}_{0.04}\text{Ni}_{0.19}\text{Mn}_{0.7}\text{O}_2$, $\text{P2-Na}_{0.78}\text{Co}_{1/2}\text{Mn}_{1/3}\text{Ni}_{1/6}\text{O}_2$, $\text{P2-Na}_{0.5}\text{Mg}_x\text{Ni}_{0.17-x}\text{Mn}_{0.87}\text{O}_2$ ($x = 0, 0.02, 0.05$ and 0.07), $\text{P3-Na}_{0.67}\text{Ni}_{0.2}\text{Mg}_{0.8}\text{O}_2$ and $\text{P3-Na}_{0.6}\text{Mg}_{0.2}\text{Mg}_{0.8}\text{O}_2$. The aim of these studies was to analyze the materials in different states of charges with a variety of spectroscopic techniques. Different redox contributions during cycling are studied in order to identify the cause of capacity fading and irreversible capacity losses. The results presented in this section are based on *Paper III-VII*.

4.2.1 Capacity losses in cathodes

Figure 12 shows galvanostatic cycling results for different manganese-based cathode materials to illustrate the irreversible capacity losses in the first cycles and capacity fading throughout cycling. For $\text{P2-Na}_{0.56}\text{Mg}_{0.04}\text{Ni}_{0.19}\text{Mn}_{0.7}\text{O}_2$ in *Paper III*, three voltage plateaus at 3.4 V, 3.8 V and 4.3 V can be identified during the first charging cycle (Figure 12a), which is in agreement with previous studies on similar manganese-based cathode materials such as $\text{Na}_{2/3}\text{Mg}_{0.05}\text{Ni}_{0.25}\text{Mn}_{0.7}\text{O}_2$ and $\text{Na}_{2/3}\text{Ni}_{1/3}\text{Mn}_{2/3}\text{O}_2$ [33,41,43]. The galvanostatic cycling curve during the first cycle and the following cycles look similar, despite the charge capacity loss after the first cycle: from 136 mAh/g (which is equivalent to 0.41 Na^+ removal), to 128 mAh/g in the second charging cycle.

Those capacity losses between the initial and the subsequent cycles have also been observed in a similar cathode material, $\text{Na}_{0.78}\text{Ni}_{0.23}\text{Mn}_{0.69}\text{O}_2$, and have been suggested to be due to anionic redox contributions [41]. In CV measurements, three main redox peak regions can be identified: (i) in the range of 2.1-2.5 V, which can be due to $\text{Mn}^{3+}/\text{Mn}^{4+}$ redox reactions, (ii) between 3.1 and 3.8 V which can correspond to $\text{Ni}^{2+}/\text{Ni}^{4+}$ processes and (iii) above 4.0 V, possibly related to phase transitions combined with electrolyte decomposition or other reactions such as oxygen oxidation, which has been discussed in previous reports [85–87].

Figure 12b shows the galvanostatic cycling results of $\text{P2-Na}_{0.78}\text{Co}_{1/2}\text{Mn}_{1/3}\text{Ni}_{1/6}\text{O}_2$, discussed in more details in *Paper IV*. The first charge and discharge capacities are 146 mAh/g and 143 mAh/g, corresponding to removal of 0.58 Na^+ and 0.56 Na^+ , respectively. In the first cycle, a large plateau above 4.2 V vs. Na^+/Na can be seen. That plateau decreases in the second discharge cycle implying irreversible reactions. However, the plateau remains throughout the cycling, implying a reversible reaction after the second cycle.

In Figure 12c, three different voltage ranges have been tested for $\text{P3-Na}_{0.67}\text{Ni}_{0.2}\text{Mn}_{0.8}\text{O}_2$ and the capacity is shown as a function of cycle number. The material cycled between 1.8 and 3.8 V (Figure 12c, black) exhibits a first discharge capacity of 150 mAh/g and a capacity retention of 93% after 25 cycles. With a higher voltage range of 1.8-4.1 V, a higher discharge capacity of 174 mAh/g with a lower capacity retention of 83% after 25 cycles is obtained. When cycled between 1.8 and 4.4 V, the initial discharge capacity is the higher (204 mAh/g) at the expense of its capacity retention (49% over 25 cycles). Hence, if the sample is charged above 4.0 V, the cycle life will be shortened significantly. In the differential capacity plots, the material with a voltage range of 1.8-3.8 V shows reversible reactions at 1.95, 2.15, 3.27 and 3.57 V. When the cutoff potential is increased to 4.1 V, an irreversible peak is seen at 4.0 V. With higher a cutoff potential of 4.4 V, new oxidation and reduction peaks occur between 4.1 and 4.3 V. The redox peaks at the highest voltage ranges decrease with cycle number, corresponding to the capacity fading observed in Figure 12c.

Figure 12d shows the capacity fading of two different types of $\text{P3-Na}_{0.67}\text{Mg}_{0.2}\text{Mn}_{0.8}\text{O}_2$, synthesized in air ($\text{Air-Na}_{0.67}\text{Mg}_{0.2}\text{Mn}_{0.8}\text{O}_2$) or oxygen ($\text{Oxy-Na}_{0.67}\text{Mg}_{0.2}\text{Mn}_{0.8}\text{O}_2$). The capacity fading, as seen in Figure 12d, is more significant due to a higher voltage window of 1.8-4.3V, whereas with a smaller range of 1.8-3.8 V a more stable cycling performance and a higher capacity retention of 96% can be observed.

Galvanostatic cycling results of $\text{P2-Na}_{0.5}\text{Mg}_x\text{Ni}_{0.17-x}\text{Mn}_{0.83}\text{O}_2$ ($0 \leq x \leq 0.07$) are shown in Figure 12e. The specific capacity for samples with Mg-content of $x=0.02$ and $x=0.05$ show a higher charge capacity in the second cycle than in the first cycle, implying that more Na is inserted during discharge in order

to be removed in the second charging cycle. For comparability, capacity retention is therefore shown relative to cycle 2. In general, the sample with Mg content $x=0.02$ shows the highest specific charge capacity in the second charging cycle (~ 160 mAh/g) and the highest charge capacity retention (97% over 8 cycles). With higher Mg content ($x=0.05, 0.07$), the second cycle charge capacity decreases and a lower capacity retention over 8 cycles is observed. The Mg-free sample showed a high initial charge capacity of 155 mAh/g but compared to Mg-doped samples, the Mg-free sample has the lowest capacity retention of 87% over 8 cycles.

Possible causes for such capacity fadings over cycle time in different manganese-based cathode materials include: structural changes, anionic/cationic contributions, diffusion limiting processes and electrolyte oxidation.

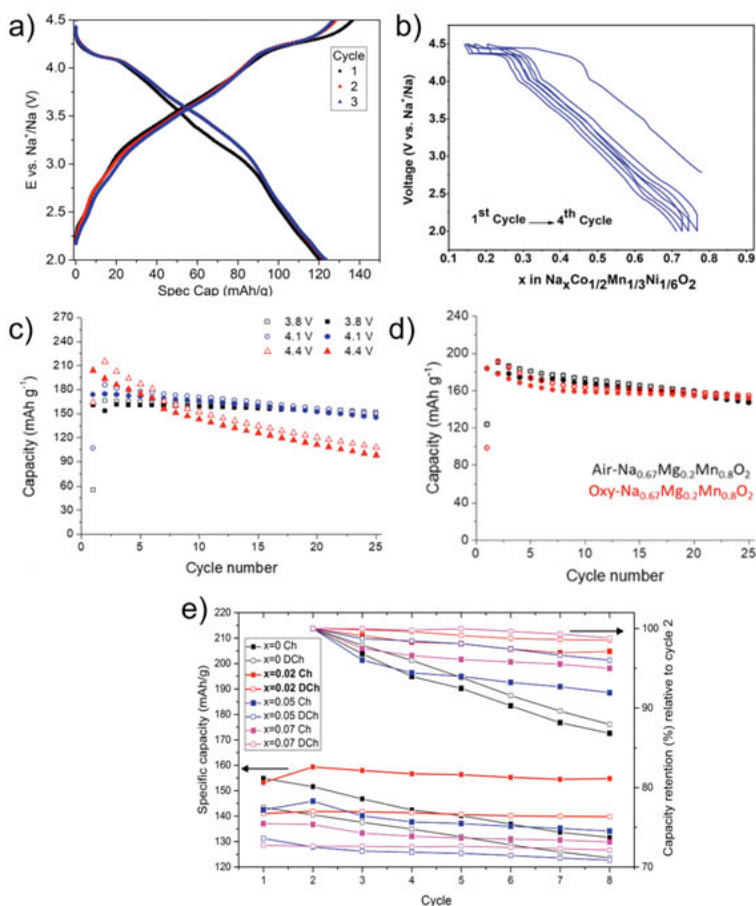


Figure 12. Irreversible capacity losses and capacity fading in different manganese-based cathodes. a) Electrochemical testing of P2- $\text{Na}_{0.56}\text{Mg}_{0.04}\text{Ni}_{0.19}\text{Mn}_{0.70}\text{O}_2$ from Paper III. Potential as a function of specific capacity during the first three cycles at 0.1 C rate with irreversible capacity loss in the first sodiation cycle. b) Electrochemical performance of P2- $\text{Na}_{0.78}\text{Co}_{1/2}\text{Mn}_{1/3}\text{Ni}_{1/6}\text{O}_2$ from Paper IV. Galvanostatic cycling during first four cycles using a current density of 25 mA/g in a potential window of 2.0 to 4.5 V with a large plateau in the first cycle indicating irreversible capacity loss. c) Galvanostatic cycling results for P3- $\text{Na}_{0.67}\text{Ni}_{0.2}\text{Mn}_{0.8}\text{O}_2$ from Paper V. Capacity plotted against the cycle number with different voltage ranges of 1.8-3.8 V (black), 1.8-4.1 V (blue) and 1.8-4.4 V (red) at a rate of 10 mA/g. Empty symbols correspond to charge, whereas full symbols represent discharge capacities. With a voltage range of 1.8-4.4 V, a faster capacity fading is observed compared to smaller voltage ranges. d) Galvanostatic cycling results of P3- $\text{Na}_{0.6}\text{Mg}_{0.2}\text{Mn}_{0.8}\text{O}_2$ from Paper VI, synthesized either in air or oxygen atmosphere. Capacity fading was observed with a cycling voltage range of 1.8-4.3 V at a rate of 10 mA/g. e) Galvanostatic measurements of P2- $\text{Na}_{0.5}\text{Mg}_x\text{Ni}_{0.17-x}\text{Mn}_{0.83}\text{O}_2$ ($0 \leq x \leq 0.07$) from Paper VII cycled at 0.1C in the range of 2-4.5 V, shown as the specific capacity versus cycle number and the capacity retention over 8 cycles relative to cycle 2. The solid symbols represent the charging capacities, whereas the empty symbols the discharge capacities. The highest capacity fading was observed without Mg-doping (black).

4.2.2 Elements affecting capacity loss at the cathode

This chapter highlights the factors contributing to capacity losses/fading observed in 4.2.1.

4.2.2.1 Electrolyte stability

Electrolyte stability can also affect the cycling stability as shown in Figure 13 for P2- $\text{Na}_{0.56}\text{Mg}_{0.04}\text{Ni}_{0.19}\text{Mn}_{0.7}\text{O}_2$ and P3- $\text{Na}_{0.67}\text{Mg}_{0.2}\text{Mn}_{0.8}\text{O}_2$ from *Paper III* and *VI*, respectively. XAS measurements at the K-edge give information on the O $1s$ core electrons which are excited to unoccupied states above the Fermi level. Figure 13a show surface-sensitive TEY as well as bulk-sensitive TFY and PFY O K-edge spectra of P2- $\text{Na}_{0.56}\text{Mg}_{0.04}\text{Ni}_{0.19}\text{Mn}_{0.7}\text{O}_2$. The pre-edge, which ranges from 528.5 to 533.0 eV, corresponds to O $2p$ orbitals, mainly hybridized with TM $3d$ orbitals, whereas peaks above 533 eV are attributed to excitations of O $2p$ orbitals hybridized with TM $4s$ and $4d$ orbitals. In Figure 13a, the TEY spectra show upon desodiation (from pristine to *1-Ch: 4.5 V*) a gradual peak increase at 532 eV and hence more surface oxygen hole states likely exists. When resodiating to sample *1-DCh: 2.0V*, the low-energy peak is completely filled, but is empty again after the second desodiation (*2-Ch: 4.5 V*). In contrary, the bulk sensitive spectra on the O K-edge do not show any significant changes during cycling. Such discrepancies in electronic structures between surface and bulk have also been observed for P2- $\text{Na}_{0.78}\text{Co}_{1/2}\text{Mn}_{1/3}\text{Ni}_{1/6}\text{O}_2$, which can originate from extra charge consumption due to electrolyte decomposition [26,42]. Hence, such electrolyte decompositions on the electrode surface as shown in Figure 13b and c can add to irreversible capacity losses, as seen for P2- $\text{Na}_{0.56}\text{Mg}_{0.04}\text{Ni}_{0.19}\text{Mn}_{0.7}\text{O}_2$ (Figure 12a), and capacity fading, as observed for P3- $\text{Na}_{0.67}\text{Mg}_{0.2}\text{Mn}_{0.8}\text{O}_2$ (Figure 12d). Thus, it is important to investigate the electrolyte stability to ensure limited capacity losses.

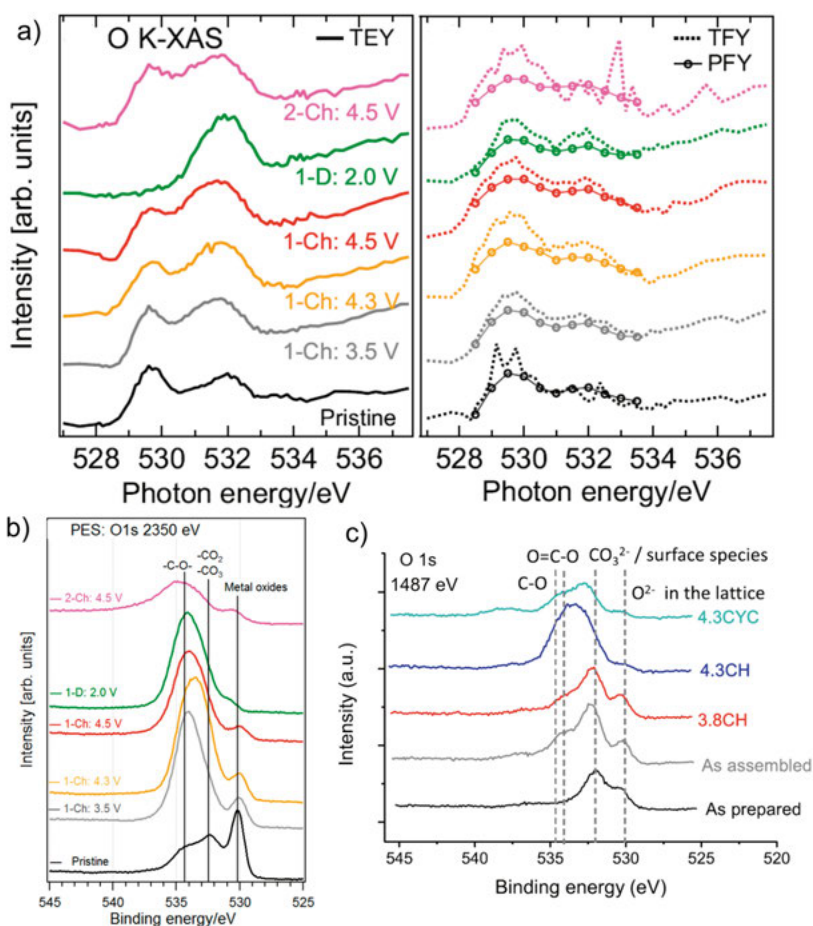


Figure 13. Surface effects of electrolyte decomposition. a) XAS spectra of O K-edge in $P2\text{-Na}_{0.56}\text{Mg}_{0.04}\text{Ni}_{0.19}\text{Mn}_{0.7}\text{O}_2$ from Paper III with surface sensitive TEY mode and bulk sensitive TFY and PFY mode. Comparison between surface and bulk sensitive spectra show differences in peak intensities. b) Surface sensitive O 1s XPS analysis on $P2\text{-Na}_{0.56}\text{Mg}_{0.04}\text{Ni}_{0.19}\text{Mn}_{0.7}\text{O}_2$ highlight electrolyte decomposition, which could lead to the observed surface and bulk differences in a). c) Surface sensitive O 1s XPS spectra of $\text{Air-Na}_{0.67}\text{Mg}_{0.2}\text{Mn}_{0.8}\text{O}_2$ from Paper VI also demonstrate electrolyte decomposition at high voltages.

4.2.2.2 Cationic and anionic redox mechanisms

Anionic contributions such as oxygen redox activities can also affect the cycling performance. In order to have a better comprehension of the role of oxygen redox during cycling, RIXS measurements with incident photon energies over pre-edge regions were performed. RIXS spectra are based on the emission from occupied O $2p$ to O $1s$ bands which depends strongly on the electronic nature and chemical state of oxygen. Figure 14 shows RIXS spectra of

the O K-edge measured for different cathode materials from *Paper III, IV* and *V* to probe the electronic structure of oxygen upon cycling.

As seen in P2-Na_{0.56}Mg_{0.04}Ni_{0.19}Mn_{0.7}O₂ (Figure 14a), the two arrows show the evolution of a low-energy peak at the end of the first desodiation. After resodiation, the peak disappears and reappears at the second desodiation. This is similar to reports on Li-rich materials and Na_{2/3}Mg_{0.28}Mn_{0.72}O₂ [40,88]. Contrary to that, Figure 14a does not exhibit an elastic peak, which would have been related to localized oxygen species which can undergo reversible anionic redox processes. This could suggest the presence of delocalized O *2p* states, which is due to an enlarged oxygen hybridization. Moreover, the RIXS spectra of the pristine sample have a more asymmetric character compared to the resodiated sample (*I-DCh: 2.0 V*). This could be related to the different distribution of redox processes observed between Mn and Ni, as discussed in *Paper III*. During the first charging cycle, only Mn undergoes redox, whereas in the second charging cycle both Mn and Ni participate in the redox process which could affect the electronic nature of bulk oxygen ions.

In P2-Na_{0.78}Co_{1/2}Mn_{1/3}Ni_{1/6}O₂ (Figure 14b) from *Paper IV*, the evolution of the O K-edge RIXS spectra is slightly different. Between 4.2 and 4.5 V, a peak broadening with a growing elastic peak at 531.5 eV can be observed. This can be associated with localized, unoccupied states of the oxygen in this voltage range [38,88]. When discharged to 2.0 V, similar to P2-Na_{0.56}Mg_{0.04}Ni_{0.19}Mn_{0.7}O₂, the RIXS spectra are different from the OCV spectrum, indicating a rearrangement of lattice oxygen.

Figure 14c shows the O K-edge RIXS spectra of P3-Na_{0.67}Ni_{0.2}Mn_{0.8}O₂ with an incident energy of 530 eV. A shape change in the shoulder at 527 eV can be observed, which is related to Mn d-d excitation of constant energy loss, shown via excitation of oxygen. The peak at 525.5 eV for the sample charged to 3.8 V increases and shifts to higher energy upon charging to 4.4 V, resulting in a peak at 526 eV for sample 4.4CH. This can be associated with hybridized Ni_{3d}-O_{2p} states at high voltages. Due to the higher electronegativity of Ni⁴⁺ and the increasing number of oxygen hole states during charging, the hybridization of Ni_{3d}-O_{2p} orbitals is more favored than Mn_{3d}-O_{2p}. Hence, as discussed in detail in *Paper V*, the slight decrease in integrated pre-edge intensity from pristine samples compared to those charged to 3.8 V could be explained by the transition from hybridization with fully occupied O *2p* states in the pristine, to partially occupied O *2p* states. This is also in agreement with the sharpness of the signal around the incident energy (*i.e.* the elastic peak), seen only for the pristine sample. Such changes in the elastic peak are considered fingerprints for O *2p* state changes [26,89–91].

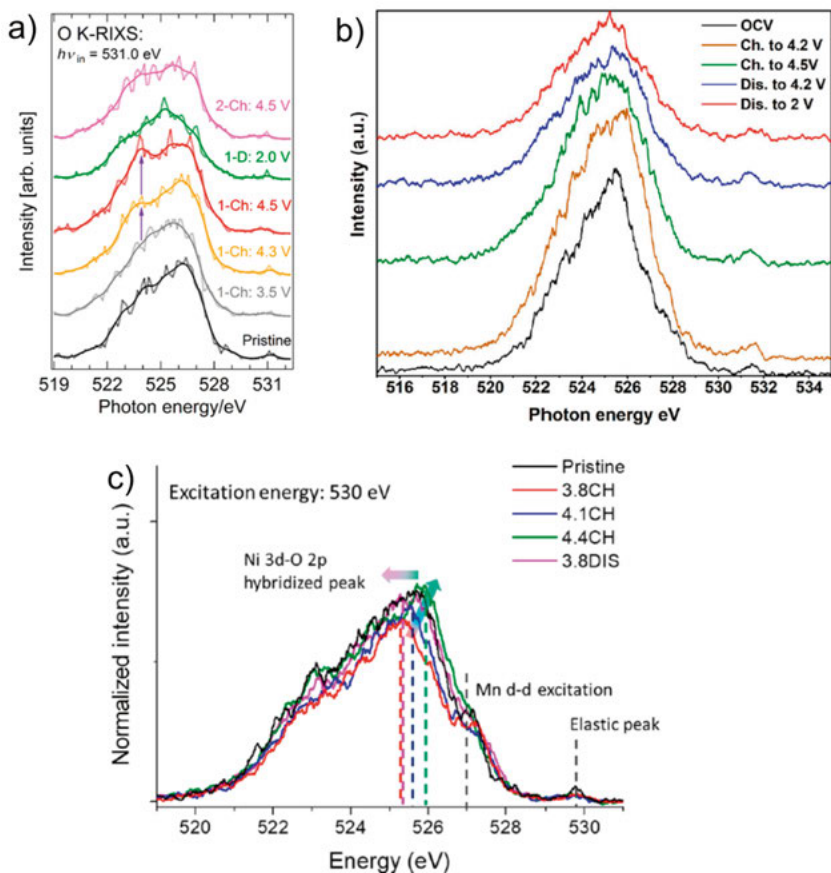


Figure 14. RIXS measurement on O K-edge to illustrate oxygen contribution at high potentials. a) O K-edge RIXS spectra of $P2\text{-Na}_{0.56}\text{Mg}_{0.04}\text{Ni}_{0.19}\text{Mn}_{0.70}\text{O}_2$ at an incident photon energy of 531.0 eV from Paper III. Evolution over the desodiation and sodiation cycles; as guide for the eye, the dashed data traces are overlaid by level 2 binomially smoothed solid traces. The emergence of a peak at 523 eV originating from an O 2p valence band emission is highlighted. b) O K-edge RIXS spectra of $P2\text{-Na}_{0.78}\text{Co}_{1/2}\text{Mn}_{1/3}\text{Ni}_{1/6}\text{O}_2$ at different states from Paper IV using an incident energy of 531.5 eV. c) RIXS analysis on the O K-edge of $P3\text{-Na}_{0.67}\text{Ni}_{0.2}\text{Mn}_{0.8}\text{O}_2$ with incident energy of 530 eV, taken from Paper V.

In conclusion, both manganese-based P2- and P3-materials demonstrate partial reversible oxygen redox activities. Different to P2 materials, P3 shows an additional reductive coupling between Ni and O at higher voltages. Such redox activities can contribute to higher capacities as seen in Figure 12c, but at the cost of cycling stability. The irreversible oxygen state changes at the initial cycles could also affect the cycling stability, leading to irreversible capacity losses. Thus, the gain of extra capacity from oxygen comes at the price of long-term cycling performance and therefore needs to be carefully considered.

4.2.2.3 Structural stability

Structural changes at potentials above 4.0 V are, for instance, observed in $\text{P2-Na}_{0.56}\text{Mg}_{0.04}\text{Ni}_{0.19}\text{Mn}_{0.7}\text{O}_2$. Even though the substitution of Mn with Ni and Mg should improve the long-term cyclability, the material still shows irreversible capacity losses in the initial cycles. In general, at high voltages, it undergoes a phase transition from P2 to the OP4 phase, which is an intergrowth structure between P2 and O2 structures. However, the XRD results in Figure 15 from *Paper III* reveal that during the first cycle at 4.5 V, the P2 and the newly formed OP4 phase are both present, meaning that the P2 is not completely formed to OP4. In the subsequent cycles, the P2 phase diminishes at high voltages, while only the OP4 phase remains. Hence, the coexisting phases in the initial cycle could contribute to such irreversible capacity losses as seen in Figure 12a. To minimize such irreversible losses, such material should be cycled more careful in the initial cycle to ensure complete phase transition from P2 to OP4. Another approach could be substituting Mn and Ni with different metals, resulting in more reversible and efficient phase transitions when cycling at higher voltages.

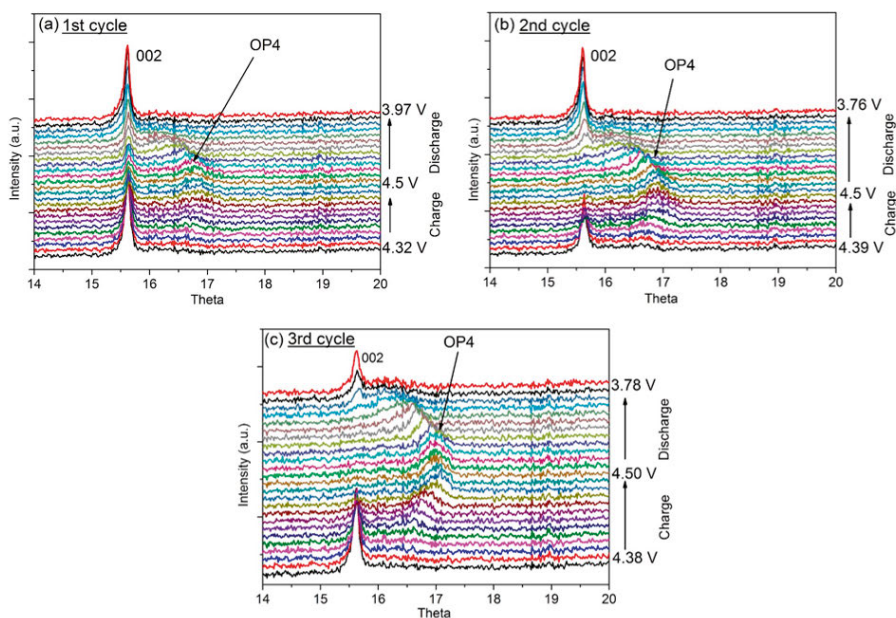


Figure 15. In situ XRD patterns of $\text{P2-Na}_{0.56}\text{Mg}_{0.04}\text{Ni}_{0.19}\text{Mn}_{0.7}\text{O}_2$ from *Paper III* cycled galvanostatically in a half-cell at a rate of 15 mA/g. a) XRD pattern during first cycle. The 002 peak corresponding to a P2 phase is still present, while the OP4 phase is formed at high voltages. b) XRD pattern during the second cycle. The peak related to the P2 phase is diminished at high voltages, while the OP4 phase is formed. c) XRD pattern during third cycle. As in the second cycle, only the OP4 phase is present at high voltage, suggesting that the first cycle showed an incomplete phase transition.

Another important factor for capacity fading is the effectiveness of desodiation/sodiation of the material – in other words, cycling reversibility. One method to measure the reversibility at a certain voltage range is the anodic and cathodic peak potential difference E_{diff} obtained from CV measurements as shown in Figure 16 for $\text{P2-Na}_{0.5}\text{Mg}_x\text{Ni}_{0.17-x}\text{Mn}_{0.83}\text{O}_2$ ($0 \leq x \leq 0.07$) from *Paper VII*. The peak potential difference at around 4.2 V vs. Na^+/Na can give information on how reversible that specific redox process is. For ideal diffusion controlled processes, the peak potential difference E_{diff} should be 0.059 V [47]. If E_{diff} is larger than 0.059 V, the process is defined as quasi-reversible. The smaller the value for E_{diff} , the more reversible the redox process. For $\text{P2-Na}_{0.5}\text{Mg}_x\text{Ni}_{0.17-x}\text{Mn}_{0.83}\text{O}_2$ ($0 \leq x \leq 0.07$) from *Paper VII*, the smallest peak potential difference at around 4.2 V vs. Na^+/Na is observed for the undoped sample and with a Mg content of $x=0.02$. From Figure 12e, the Mg-doped sample $x=0.02$ also showed the best capacity retention. However, there is a discrepancy for the Mg-free sample between the galvanostatic results in Figure 12e and the CV results in Figure 16, which could be due to the negligence of the peak current, which is not considered for E_{diff} analysis.

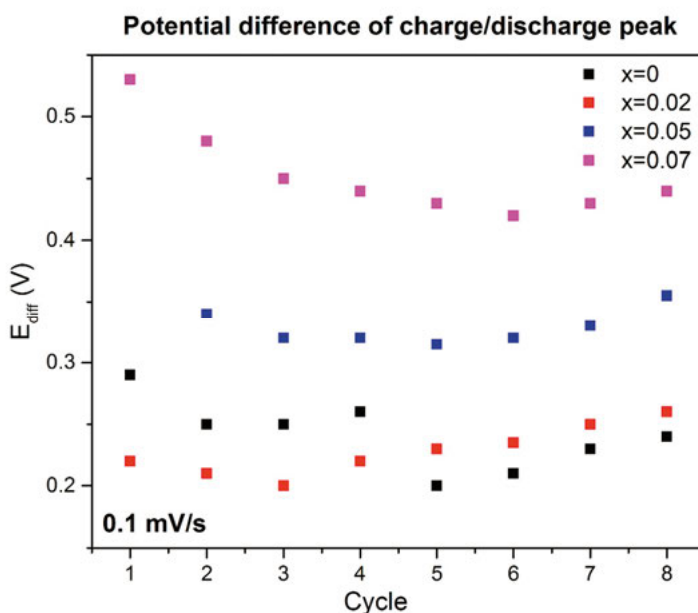


Figure 16. Cyclic voltammetry results of $\text{P2-Na}_{0.5}\text{Mg}_x\text{Ni}_{0.17-x}\text{Mn}_{0.83}\text{O}_2$ ($0 \leq x \leq 0.07$) from *Paper VII* measured at a scan rate of 0.1 mV/s. The differences between anodic and cathodic peak potential at around 4.2 V vs. Na^+/Na (E_{diff}) are plotted as a function of cycle number.

4.2.2.4 Na-diffusion

Not only the redox activities of the transition metals need to be studied, as in *Paper III-VI*, but also the Na-diffusion needs to be considered. The Na-ion diffusion can be a limiting factor for the cycling to understand how cycling stability correlates with Na-mobility, the initial chemical diffusion coefficient of Na-ions from galvanostatic intermittent titration technique (GITT) measurements were determined after the first current pulse by using equation Eq. 1 (see section 3.1) and is shown in Figure 17a. According to the GITT results, Mg-contents of $x=0.02$ delivered the highest diffusion coefficient ($D_{\text{Na},\text{in}}^{\text{G}} = 5.4 \times 10^{-10} \text{ cm}^2/\text{s}$) which is in alignment with the electrochemical results in Figure 12e, where $x=0.02$ exhibits the highest capacity and capacity retention. Hence, the sample with the most favorable cycling stability also exhibits the highest initial Na-mobility. There are discrepancies between pristine (Figure 17b) and cycled samples (Figure 17a), as there is a difference in chemical diffusion and self-diffusion behaviour. The combination of electrochemical and $\mu^+\text{SR}$ experiments enabled to identify the sample with the highest Na-mobility, as in large values for chemical diffusion and self-diffusion constants. Consequently, a high Na-mobility can enhance the cycling stability.

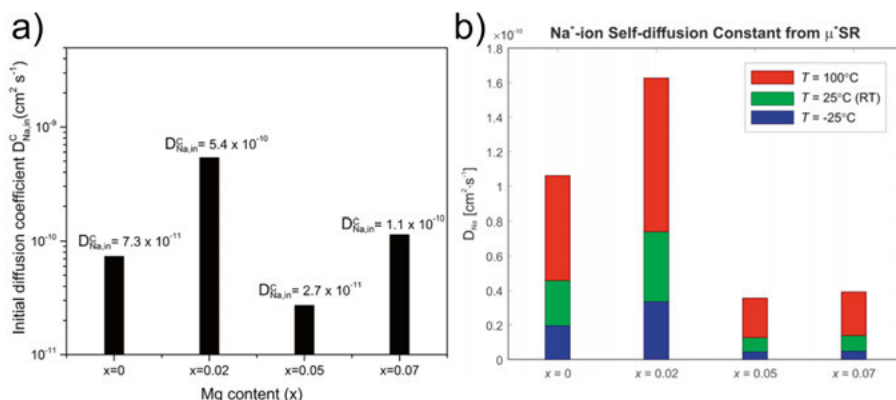


Figure 17. GITT and $\mu^+\text{SR}$ results on $\text{P2-Na}_{0.5}\text{Mg}_x\text{Ni}_{0.17-x}\text{Mn}_{0.83}\text{O}_2$ ($0 \leq x \leq 0.07$) from Paper VII. a) Initial chemical diffusion coefficients of Na-ions determined after the first current pulse based on GITT measurements. b) Self-diffusion constants based on the $\mu^+\text{SR}$ results.

5. Conclusion and future work

In this thesis, different electrochemical and spectroscopy techniques have been utilized to understand ageing mechanisms at in SIBs. At the anode/electrolyte interface, a variety of electrolyte systems have been tested, in order to understand the fundamentals of capacity losses stemming from SEI dissolution and Na-loss processes such as Na-ion trapping. On the cathode side, the ageing mechanisms in different manganese-based cathode materials upon electrochemical cycling were investigated.

The studies in *Paper I* and *II* on reactions at the anode/electrolyte interface provided new insight to understand the major challenges regarding ageing in SIB research. The usage of a specific cell setup with different working electrodes and various cycling protocols to comparatively study electrochemical properties in different electrolytes enabled us to separate capacity loss contributions in SEI dissolution and Na-loss related to SEI reformation and Na-ion trapping. The implementations of open-circuit pauses in between cycling sequences helped to analyze self-discharge during pause due to SEI ageing. Coupled with XPS measurements, the results shed light on different ageing mechanism during pause, defined by electrolyte salt and solvent. For example, the choice of electrolyte salt significantly affects the SEI development (growth or dissolution) during pause, whereas the electrolyte solvent is significantly affecting the magnitude of capacity loss during cycling and after pause. The study in *Paper II* underlines the importance of electrolyte matrix and its influence on the SEI, as well as the powerful usage of cycling protocols to measure different capacity loss contributions. Additionally, the effects of unconventional additives, *i.e.* Na_2CO_3 and NaF, were studied. The presence of NaF in the electrolyte results in an inclusion of NaF in the SEI in 1 M $\text{NaPF}_6\text{-PC}$, which led to less capacity loss and hence, a more stable SEI. These results open up new opportunities to investigate saturation of electrolyte solution with possible SEI species to mitigate SEI dissolution. Such unconventional additives, like NaF from *Paper I*, successfully prevented SEI dissolution. This can in particular be continued to formulate effective organic and inorganic additive to address ageing in rechargeable batteries. Though the focus of this thesis was on SIBs, the methods and guidelines used here can be used to address ageing in similar battery chemistries including lithium-ion batteries.

Using a complementary range of X-ray spectroscopy techniques provided extended insights on the failure mechanism in manganese cathode materials, as shown in *Paper III-VII*. Surface-sensitive XPS analyses on P2-

$\text{Na}_{0.56}\text{Mg}_{0.04}\text{Ni}_{0.19}\text{Mn}_{0.7}\text{O}_2$ and $\text{P3-Na}_{0.67}\text{Mg}_{0.2}\text{Mn}_{0.8}\text{O}_2$ have shown significant electrolyte decomposition at the electrode surface, which induced dissimilar redox behaviours between the surface and bulk, as seen for $\text{P2-Na}_{0.56}\text{Mg}_{0.04}\text{Ni}_{0.19}\text{Mn}_{0.7}\text{O}_2$, contributing to additional capacity loss.

Besides the cationic TM redox activity, also the charge uptake of anionic contributions needs to be considered. XAS and RIXS analysis on the O K-edge in $\text{P2-Na}_{0.56}\text{Mg}_{0.04}\text{Ni}_{0.19}\text{Mn}_{0.7}\text{O}_2$, $\text{P2-Na}_{0.78}\text{Co}_{1/2}\text{Mn}_{1/3}\text{Ni}_{1/6}\text{O}_2$ and $\text{P3-Na}_{0.67}\text{Ni}_{0.2}\text{Mn}_{0.8}\text{O}_2$ showed that the electronic nature of oxygen undergoes a rearrangement during the first cycle, corresponding to the anionic contribution in the redox processes. Additionally, $\text{P3-Na}_{0.67}\text{Ni}_{0.2}\text{Mn}_{0.8}\text{O}_2$ showed a reductive coupling between nickel and oxygen redox upon charging. At high voltages, cathode materials can undergo incomplete phase transitions, which can result in irreversible capacity losses as shown for $\text{P2-Na}_{0.56}\text{Mg}_{0.04}\text{Ni}_{0.19}\text{Mn}_{0.7}\text{O}_2$. Such findings on different redox contributions (both cationic and anionic) and insufficient phase transitions are instrumental and should be taken into account if constructing a full cell, to compensate additional or missing charge uptake.

Moreover, the μ^+ SR technique was used to understand the correlation between Na-mobility and cycling stability in $\text{P2-Na}_{0.5}\text{Mg}_x\text{Ni}_{0.17-x}\text{Mn}_{0.83}\text{O}_2$ ($0 \leq x \leq 0.07$). The sample with Mg-content of $x=0.02$ exhibited the best cycling stability according to the electrochemical results. Furthermore, with GITT, the highest initial chemical diffusion coefficient of Na-ion was found for $x=0.02$ Mg-content. This agrees with the determined self-diffusion coefficient calculated from μ^+ SR results of the pristine powder, where the sample with $x=0.02$ Mg-content also showed one of the highest constants amongst the samples. Hence, for a better long-term cycling stability, a high Na-diffusion coefficient is desired.

Summing up, the failure mechanisms of SIBs are highly complex, which require complementary powerful techniques to have a better understanding of ageing mechanisms. Understanding what leads to failure at the cathode and anode site is essential to prolong the life-time of sodium-ion batteries.

Future work should focus on extending this framework into new methods to scrutinize different ageing processes. The concept of new cycling protocols with pauses should be used for future studies to explore SEI ageing processes at a deeper level. Furthermore, the use of unconventional additives to saturate the electrolytes showed a different aspect of additive chemistry to prevent SEI dissolution. Future additive research could focus on using cycled or aged electrolyte containing a high concentration of dissolved SEI components, which could be added to the target electrolyte system to notably minimize SEI dissolution. Complimentary techniques to galvanostatic experiments have shown to be helpful to understand capacity fading in cathode materials, so the methods can be utilized to either design new materials or to prevent electrode ageing of cathode materials -*i.e.*, to truly master anti-ageing strategies.

As the understanding of ageing in SIB technology increases, so should the cycling lifetimes of SIBs. This would make the SIB technology competitive with its lithium analogue, due to generally costly material resources and fabrication of the batteries. Once there are solutions to solve battery ageing at laboratory research level, the next challenge awaits to move from laboratory scale to industrial large-scale applications while preserving cost-effective and environmentally friendliness of materials. Such future goal is not easy, because the parameters used in research labs are often different from those in industry. However, current technologies in lithium-ion batteries have shown that all such obstacles can be overcome with time and more research. Therefore, there is a hope for sodium-ion batteries to compete with lithium-ion batteries for some specific yet highly important applications such as stationary storage.

6. Acknowledgements

First of all, thank you for reading this thesis, even though you might have just skipped all the pages to read the acknowledgements –cheers!

I would like to thank all of my co-authors for making all of this work possible. A big thanks to Daniel Brandell for being my second supervisor -for your help and input I received in general for this work.

Thank you, Leif, for all your comments and discussions. My work would not be as good as without your help and input.

I would like to thank Laurent Duda for being my third supervisor, the “sensei” in physics. Danke für all deine Hilfe und deine Geduld. Trotz Jetlag oder langer Anreise, hattest du dennoch immer ein offenes Ohr für mich während und nach jeder Strahlzeit–danke!

Reza, I could not wish for a better main supervisor! Thank you for giving me all these opportunities and giving me this PhD project. This has been one of the most exciting part of my life – danke!

To my colleagues from ÅABC and at Ångström lab, thank you for the fruitful discussions, motivational peptalks and detox sessions. You all truly made this one of the best memories in my life, during work and outside. CHEERS!

Thanks to my friends all over the world, especially in Sweden and Germany for their unconditional support offline and online. I would like to thank you, Marie, for starting this amazing journey with me in Sweden including all the moments with sad and happy tears. Jay, Ghanim, and Jarvis, you guys made my life so much more colourful and always filled with a lot of “tea”. Sara, my queen, thank you for your sass, which kept me going. Sandy, thanks for your peptalks and keeping my head clear, even though you are so far away. Danke an meine Freunde zu Hause in Deutschland: Duc, Giang, Viet Au, Trung, Hoan, Sophie und Enise. I would like to thank my fabulous Stockholm guys Chen, Linus, Martin and Henrik.

Thank you, Keng. For showing continuous support and care. You always know how to cheer me up and keep me motivated.

Cảm ơn Bố Mẹ và Ceng und Alti. Ceng, jetzt bist du dran. Danke für die Feierabendanrufe auf meinem Fahrrad und die tiefgründigen Unterhaltungen über meine Wocheneinkäufe – mit Alti. Không ai bằng Bố Mẹ. Cảm ơn Bố Mẹ nhiều, để cho con thành công và được rất nhiều túi -keke.

Yours truly, Le Anh.

7. Sammanfattning på svenska

Batterier utgör en av de viktigaste teknologierna för energilagring som kommer att möjliggöra att samhället blir mer miljövänligt. Genom att lagra elektricitet från förnybara energikällor kan samhället fasa ut fossila bränslen. Utvecklingen av batterier kommer att resultera i en växande efterfrågan för denna energilagringsteknik. Laddningsbara batterier som t.ex. litium-jonbatterier spelar en viktig roll inom bärbar elektronik, såväl som i bilindustrin på grund av deras utmärkta energi- och effekttäthet i jämförelse med andra batteriteknologier. Konventionella batteriers prestanda skiljer sig kraftigt beroende på valet av elektrodmaterial och elektrolytsammansättning. I litium-jonbatterier används t.ex. litiumkoboltoxid ofta som katodmaterial. Detta är bakgrunden till att teknologin blivit mer och mer ifrågasatt från ett resursperspektiv. Litiumkoboltoxid har valts på grund av dess utmärkta prestanda och har varit svårt att ersätta utan att kompromissa med batteriets dess kapacitet och/eller stabilitet. Koboltmaterial är dock förknippade med stora resursproblem. Kobolt är mindre tillgängligt och dyrare jämfört med andra övergångsmetaller samtidigt som koboltanvändningen även är problematisk ur en politisk och etisk synvinkel, då mycket kobolt bryts i odemokratiskt styrda regioner i Afrika.

Därutöver kan den förväntade ökade efterfrågan på batterier på längre sikt leda till kapacitetsproblem eftersom världens litiumresurser också är begränsade. Med detta i åtanke kan natrium-jonbatterier vara ett bra alternativ med avseende på kostnadseffektivitet och hållbarhet. Natrium är ett av de mest förekommande element på jorden, och det går att konstruera kobolt-fria batterier baserade på natrium. Jämfört med litium-jonbatterier har emellertid natrium-jonbatterier i genomsnitt en lägre energitäthet. För stationära batteri-applikationer är energitätheten dock inte lika viktig som kostnad och hållbarhet. Lång livslängd är däremot av yttersta vikt för att uppnå en hållbar användning i framtida storskaliga applikationer. Jämfört med litium-jonbatterier är forskningen kring natrium-jonbatterier inte lika välutvecklad. För att kunna använda natrium-jonbatterier i framtida applikationer där lång livstid krävs är det nödvändigt att förstå vad som kan leda till kapacitetsminskningar och hur sådana mekanismer kan förhindras. I detta arbete beskrivs dessa problematiska mekanismer vid både katoden samt i gränsskiktet mellan anod och elektrolyt med hjälp av en mängd olika spektroskopiska och elektrokemiska metoder.

Interaktionerna mellan anod och elektrolyt har undersökts i detalj med hjälp av galvanostatisk cykling, där flera olika cyklingsprotokoll samt fotoelektron-spektroskopi (XPS) använts. Elektrolytens komponenter bryts ned vid låga potentialer och bildar därigenom en passiveringsfilm på anodens yta, det är denna film som kallas ”SEI” (Solid Electrolyte Interphase). Ett idealt SEI skall vara kemiskt stabilt och olösligt, men tyvärr är SEI-lagret i natrium-jonbatterier mer lösligt än i litium-jonbatterier. Ett instabilt SEI kan orsaka kapacitetsförluster under cykling och på så sätt minska batteriets hållbarhet. SEI-stabiliteten i flera elektrolytssystem har utvärderats, både under och efter pauser i cyklingen, och därtill har även effekterna av olika tillsatser som syftar till att förhindra SEI-lagrets löslighet analyserats.

Därutöver har manganbaserade katoder studerats mot bakgrund av den rikliga tillgången av mangan i jordskorpan samt dessa materials lovande elektrokemiska prestanda vid höga potentialer. Analysteknikerna inkluderar synkrotronbaserad XPS, röntgenabsorptionsspektroskopi (XAS), resonant inelastisk röntgen spridningsmätningar (RIXS), samt muonspinnrelaxation i kombination med olika elektrokemiska tekniker. Dessa visade att katodmaterialet vid höga potentialer genomgår kristallstrukturförändringar som kan leda till kapacitetsförluster. Dessutom finns det ytterligare bidrag av redox-mekanismer från övergångsmetaller och särskilt syre i materialen. Oxidation av syre kan ge extra kapacitet vid höga potentialer, men till priset av elektrolytsönderfall och strukturförändringar. Detta kunde observeras via XPS och röntgendiffraktion (XRD). Med XAS- and RIXS-metoder kan just redox-bidraget från syre studeras i detalj. En ytterligare faktor som studerats är natriumjonens rörlighet, det vill säga hur snabbt natriumjoner kan röra sig i katodmaterialet. Med muonspinnrelaxation och elektrokemiska mätningar kunde diffusionen av natriumjoner i olika katoder bestämmas.

Sammantaget har resultaten i denna avhandling visat hur olika parametrar, som elektrolytssystem och redox-mekanismer, kristallstrukturförändringar och jondiffusion kan påverka kapacitetsförlusterna och därmed förkorta batteriets livslängd. Genom att skraddarsy dessa parametrar kan dock livslängden öka avsevärt, och förhoppningen är att denna forskning kan bidra till att realisera mer stabila natrium-jonbatterier.

8. References

1. Ambrose, H., and Kendall, A. (2020) Understanding the future of lithium: Part 1, resource model. *J. Ind. Ecol.*, **24** (1), 80–89.
2. Broussely, M., Biensan, P., Bonhomme, F., Blanchard, P., Herreyre, S., Nechev, K., Staniewicz, R.J., Choi, S.S., and Lim, H.S. (2005) Main aging mechanisms in Li ion batteries. *J. Power Sources*, **111** (1), 130–136.
3. Choi, S.S., and Lim, H.S. (2002) Factors that affect cycle-life and possible degradation mechanisms of a Li-ion cell based on LiCoO₂. *J. Power Sources*, **111** (1), 130–136.
4. Palomares, V., Serras, P., Villaluenga, I., Hueso, K.B., Carretero-González, J., and Rojo, T. (2012) Na-ion batteries, recent advances and present challenges to become low cost energy storage systems. *Energy Environ. Sci.*, **5** (3), 5884–5901.
5. Birkel, C.R., Roberts, M.R., McTurk, E., Bruce, P.G., and Howey, D.A. (2017) Degradation diagnostics for lithium ion cells. *J. Power Sources*, **341**, 373–386.
6. Xu, K. (2014) Electrolytes and interphases in Li-ion batteries and beyond. *Chem. Rev.*, **114** (23), 11503–11618.
7. Ponrouch, A., Monti, D., Boschini, A., Steen, B., Johansson, P., and Palacín, M.R. (2015) Non-aqueous electrolytes for sodium-ion batteries. *J. Mater. Chem. A*, **3** (1), 22–42.
8. Peled, E. (1979) The Electrochemical Behavior of Alkali and Alkaline Earth Metals in Nonaqueous Battery Systems—The Solid Electrolyte Interphase Model. *J. Electrochem. Soc.*, **126** (12), 2047–2051.
9. Peled, E., and Menkin, S. (2017) Review—SEI: Past, Present and Future. *J. Electrochem. Soc.*, **164** (7), A1703–A1719.
10. Peled, E., Golodnitsky, D., and Ardel, G. (1997) Advanced Model for Solid Electrolyte Interphase Electrodes in Liquid and Polymer Electrolytes. *J. Electrochem. Soc.*, **144** (8), L208.
11. Mogensen, R., Brandell, D., and Younesi, R. (2016) Solubility of the Solid Electrolyte Interphase (SEI) in Sodium Ion Batteries. *ACS Energy Lett.*, **1** (6), 1173–1178.
12. Moshkovich, M., Gofer, Y., and Aurbach, D. (2001) Investigation of the Electrochemical Windows of Aprotic Alkali Metal (Li, Na, K) Salt Solutions. *J. Electrochem. Soc.*, **148** (4), E155.
13. Komaba, S., Ishikawa, T., Yabuuchi, N., Murata, W., Ito, A., and Ohsawa, Y. (2011) Fluorinated ethylene carbonate as electrolyte additive for rechargeable Na batteries. *ACS Appl. Mater. Interfaces*, **3** (11), 4165–4168.
14. Sinha, N.N., Burns, J.C., and Dahn, J.R. (2013) Storage Studies on Li/Graphite Cells and the Impact of So-Called SEI-Forming Electrolyte Additives. *J. Electrochem. Soc.*, **160** (4), A709–A714.
15. Lu, M., Cheng, H., and Yang, Y. (2008) A comparison of solid electrolyte interphase (SEI) on the artificial graphite anode of the aged and cycled commercial lithium ion cells. *Electrochim. Acta*, **53** (9), 3539–3546.

16. Ryu, J.H., Kim, J.W., Sung, Y.E., and Oh, S.M. (2004) Failure modes of silicon powder negative electrode in lithium secondary batteries. *Electrochem. Solid-State Lett.*, **7** (10).
17. Lindgren, F., Rehnlund, D., Pan, R., Pettersson, J., Younesi, R., Xu, C., Gustafsson, T., Edström, K., and Nyholm, L. (2019) On the Capacity Losses Seen for Optimized Nano-Si Composite Electrodes in Li-Metal Half-Cells. *Adv. Energy Mater.*, **9** (33), 1901608.
18. Rehnlund, D., Lindgren, F., Böhme, S., Nordh, T., Zou, Y., Pettersson, J., Bexell, U., Boman, M., Edström, K., and Nyholm, L. (2017) Lithium trapping in alloy forming electrodes and current collectors for lithium based batteries. *Energy Environ. Sci.*, **10** (6), 1350–1357.
19. Wei, W., Ihrfors, C., Björefors, F., and Nyholm, L. (2020) Capacity Limiting Effects for Freestanding, Monolithic TiO₂Nanotube Electrodes with High Mass Loadings. *ACS Appl. Energy Mater.*, **3** (5), 4638–4649.
20. Li, Y., Lu, Y., Zhao, C., Hu, Y.S., Titirici, M.M., Li, H., Huang, X., and Chen, L. (2017) Recent advances of electrode materials for low-cost sodium-ion batteries towards practical application for grid energy storage. *Energy Storage Mater.*, **7** (January), 130–151.
21. Yabuuchi, N., Kubota, K., Dahbi, M., and Komaba, S. (2014) Research development on sodium-ion batteries. *Chem. Rev.*, **114** (23), 11636–11682.
22. Brant, W.R., Mogensen, R., Colbin, S., Ojwang, D.O., Schmid, S., Häggström, L., Ericsson, T., Jaworski, A., Pell, A.J., and Younesi, R. (2019) Selective Control of Composition in Prussian White for Enhanced Material Properties. *Chem. Mater.*, **31** (18), 7203–7211.
23. Barker, J., Saidi, M.Y., and Swoyer, J.L. (2003) A Sodium-Ion Cell Based on the Fluorophosphate Compound NaVPO₄F. *Electrochem. Solid-State Lett.*, **6** (1), A1.
24. Delmas, C., Fouassier, C., and Hagenmuller, P. (1980) Structural classification and properties of the layered oxides. *Phys. B+C*, **99** (1–4), 81–85.
25. Paulsen, J.M., and Dahn, J.R. (1999) Studies of the layered manganese bronzes, Na_{2/3}[Mn_{1-x}M_x]O₂ with M = Co, Ni, Li, and Li_{2/3}[Mn_{1-x}M_x]O₂ prepared by ion-exchange. *Solid State Ionics*, **126** (1), 3–24.
26. Ma, L.A., Massel, F., Naylor, A.J., Duda, L.C., and Younesi, R. (2019) Understanding charge compensation mechanisms in Na_{0.56}Mg_{0.04}Ni_{0.19}Mn_{0.70}O₂. *Commun. Chem.*, **2**, 125.
27. Clément, R.J., Bruce, P.G., and Grey, C.P. (2015) Review-Manganese-based P2-type transition metal oxides as sodium-ion battery cathode materials. *J. Electrochem. Soc.*, **162** (14), A2589–A2604.
28. Hasa, I., Passerini, S., and Hassoun, J. (2017) Toward high energy density cathode materials for sodium-ion batteries: investigating the beneficial effect of Aluminum doping on the P2-type structure. *J. Mater. Chem. A*, **5** (9), 4467–4477.
29. Wu, X., Xu, G.L., Zhong, G., Gong, Z., McDonald, M.J., Zheng, S., Fu, R., Chen, Z., Amine, K., and Yang, Y. (2016) Insights into the Effects of Zinc Doping on Structural Phase Transition of P2-Type Sodium Nickel Manganese Oxide Cathodes for High-Energy Sodium Ion Batteries. *ACS Appl. Mater. Interfaces*, **8** (34), 22227–22237.
30. Kim, E.J., Ma, L.A., Duda, L.C., Pickup, D.M., Chadwick, A. V., Younesi, R., Irvine, J.T.S., and Robert Armstrong, A. (2020) Oxygen Redox Activity through a Reductive Coupling Mechanism in the P3-Type Nickel-Doped Sodium Manganese Oxide. *ACS Appl. Energy Mater.*, **3** (1), 184–191.

31. Duffort, V., Talaie, E., Black, R., and Nazar, L.F. (2015) Uptake of CO₂ in Layered P2-Na_{0.67}Mn_{0.5}Fe_{0.5}O₂: Insertion of carbonate anions. *Chem. Mater.*, **27** (7), 2515–2524.
32. Lu, Z., and Dahn, J.R. (2001) In Situ X-Ray Diffraction Study of P2-Na_{2/3}[Ni_{1/3}Mn_{2/3}]O₂. *J. Electrochem. Soc.*, **148** (11), 1225–1229.
33. Singh, G., Tapia-Ruiz, N., Lopez Del Amo, J.M., Maitra, U., Somerville, J.W., Armstrong, A.R., Martinez De Ilarduya, J., Rojo, T., and Bruce, P.G. (2016) High Voltage Mg-Doped Na_{0.67}Ni_{0.3-x}Mg_xMn_{0.7}O₂ (x = 0.05, 0.1) Na-Ion Cathodes with Enhanced Stability and Rate Capability. *Chem. Mater.*, **28** (14), 5087–5094.
34. Hasa, I., Buchholz, D., Passerini, S., Scrosati, B., and Hassoun, J. (2014) High Performance Na_{0.5} [Ni_{0.23} Fe_{0.13} Mn_{0.63}]O₂ Cathode for Sodium-Ion Batteries. *Adv. Energy Mater.*, **4** (15), 1400083.
35. Yu, H., Guo, S., Zhu, Y., Ishida, M., and Zhou, H. (2014) Novel titanium-based O3-type NaTi_(0.5)Ni_(0.5)O₂ as a cathode material for sodium ion batteries. *Chem. Commun. (Camb.)*, **50** (4), 457–9.
36. Konarov, A., Choi, J.U., Bakenov, Z., and Myung, S.T. (2018) Revisit of layered sodium manganese oxides: Achievement of high energy by Ni incorporation. *J. Mater. Chem. A*, **6** (18), 8558–8567.
37. Li, B., Hu, Y., Zhao, C., Chen, L., Wang, Q., and Lu, Y. (2017) Review on anionic redox for high-capacity lithium- and sodium-ion batteries. *J. Phys. D. Appl. Phys.*, **50** (18), 183001.
38. Luo, K., Roberts, M.R., Guerrini, N., Tapia-Ruiz, N., Hao, R., Massel, F., Pickup, D.M., Ramos, S., Liu, Y.S., Guo, J., Chadwick, A. V., Duda, L.C., and Bruce, P.G. (2016) Anion Redox Chemistry in the Cobalt Free 3d Transition Metal Oxide Intercalation Electrode Li[Li_{0.2}Ni_{0.2}Mn_{0.6}]O₂. *J. Am. Chem. Soc.*, **138** (35), 11211–11218.
39. Perez, A.J., Batuk, D., Saubanère, M., Rouse, G., Foix, D., McCalla, E., Berg, E.J., Dugas, R., Van Den Bos, K.H.W., Doublet, M.L., Gonbeau, D., Abakumov, A.M., Van Tendeloo, G., and Tarascon, J.M. (2016) Strong oxygen participation in the redox governing the structural and electrochemical properties of Na-rich layered oxide Na₂IrO₃. *Chem. Mater.*, **28** (22), 8278–8288.
40. Maitra, U., House, R.A., Somerville, J.W., Tapia-Ruiz, N., Lozano, J.G., Guerrini, N., Hao, R., Luo, K., Jin, L., Pérez-Osorio, M.A., Massel, F., Pickup, D.M., Ramos, S., Lu, X., McNally, D.E., Chadwick, A. V., Giustino, F., Schmitt, T., Duda, L.C., Roberts, M.R., and Bruce, P.G. (2018) Oxygen redox chemistry without excess alkali-metal ions in Na_{2/3} [Mg_{0.28} Mn_{0.72}]O₂. *Nat. Chem.*, **10** (3), 288–295.
41. Ma, C., Alvarado, J., Xu, J., Clement, R.J., Kodur, M., Tong, W., Grey, C.P., Meng, Y.S., Kodur, M., Tong, W., Grey, C.P., and Meng, Y.S. (2017) Exploring Oxygen Activity in the High Energy P2-Type Na_{0.78}Ni_{0.23}Mn_{0.69}O₂ Cathode Material for Na-Ion Batteries. *J. Am. Chem. Soc.*, **139** (13), 4835–4845.
42. Hakim, C., Sabi, N., Ma, L.A., Dahbi, M., Brandell, D., Edström, K., Duda, L.C., Saadouni, I., and Younesi, R. (2020) Understanding the redox process upon electrochemical cycling of the P2-Na_{0.78}Co_{1/2}Mn_{1/3}Ni_{1/6}O₂ electrode material for sodium-ion batteries. *Commun. Chem.*, **3**, 9.
43. Lee, D.H., Xu, J., and Meng, Y.S. (2013) An advanced cathode for Na-ion batteries with high rate and excellent structural stability. *Phys. Chem. Chem. Phys.*, **15** (9), 3304–3312.

44. Kim, E.J., Ma, L.A., Pickup, D.M., Chadwick, A. V., Younesi, R., Maughan, P., Irvine, J.T.S., and Armstrong, A.R. (2020) Vacancy-enhanced oxygen redox reversibility in P3-type magnesium-doped sodium manganese oxide $\text{Na}_{0.67}\text{Mg}_{0.2}\text{Mn}_{0.8}\text{O}_2$. *ACS Appl. Energy Mater.*, **3** (11), 10423–10434.
45. Komaba, S., Yabuuchi, N., Nakayama, T., Ogata, A., Ishikawa, T., and Nakai, I. (2012) Study on the reversible electrode reaction of $\text{Na}(1-x)\text{Ni}(0.5)\text{Mn}(0.5)\text{O}_2$ for a rechargeable sodium-ion battery. *Inorg. Chem.*, **51** (11), 6211–20.
46. Yabuuchi, N., and Komaba, S. (2014) Recent research progress on iron- and manganese-based positive electrode materials for rechargeable sodium batteries. *Sci. Technol. Adv. Mater.*, **15** (4).
47. Reddy, T.B., and Linden, D. (2011) *Linden's Handbook of Batteries*, Mc Graw-Hill.
48. Dahn, J.R., and Smith, A.J. (2012) Delta Differential Capacity Analysis. *J. Electrochem. Soc.*, **159** (3), A290–A293.
49. Wen, C.J., Boukamp, B.A., Huggins, R.A., and Weppner, W. (1979) Thermodynamic and Mass Transport Properties of “LiAl.” *J. Electrochem. Soc.*, **126** (12), 2258–2266.
50. Weppner, W., and Huggins, R.A. (1977) Determination of the Kinetic Parameters of Mixed-Conducting Electrodes and Application to the System Li_3Sb . *J. Electrochem. Soc.*, **124** (10), 1569–1578.
51. Zhu, Y., and Wang, C. (2010) Galvanostatic intermittent titration technique for phase-transformation electrodes. *J. Phys. Chem. C*, **114** (6), 2830–2841.
52. Edström, K., Herstedt, M., and Abraham, D.P. (2006) A new look at the solid electrolyte interphase on graphite anodes in Li-ion batteries. *J. Power Sources*, **153** (2), 380–384.
53. Scofield, J.H. (1973) Theoretical photoionization cross sections from 1 to 1500 keV. *Intern. Rep. TID-4500, UC34, UCRL-51326*.
54. Painter, L.R., Arakawa, E.T., Williams, M.W., and Ashley, J.C. (1980) Optical properties of polyethylene: Measurement and applications. *Radiat. Res.*, **83** (1), 1–18.
55. Malmgren, S., Ciosek, K., Hahlin, M., Gustafsson, T., Gorgoi, M., Rensmo, H., and Edström, K. (2013) Comparing anode and cathode electrode/electrolyte interface composition and morphology using soft and hard X-ray photoelectron spectroscopy. *Electrochim. Acta*, **97**, 23–32.
56. Philippe, B. (2013) Insights in Li-ion Battery Interfaces through Photoelectron Spectroscopy Depth Profiling.
57. J. Stöhr (1992) *NEXAFS Spectroscopy*, Springer.
58. Abbate, M., Goedkoop, J.B., de Groot, F.M.F., Grioni, M., Fuggle, J.C., Hofmann, S., Petersen, H., and Sacchi, M. (1992) Probing depth of soft x-ray absorption spectroscopy measured in total-electron-yield mode. *Surf. Interface Anal.*, **18** (1), 65–69.
59. Achkar, A.J., Regier, T.Z., Wadati, H., Kim, Y.J., Zhang, H., and Hawthorn, D.G. (2011) Bulk sensitive x-ray absorption spectroscopy free of self-absorption effects. *Phys. Rev. B - Condens. Matter Mater. Phys.*, **83** (8), 2–5.
60. Henderson, G.S., de Groot, F.M.F., and Moulton, B.J.A. (2014) X-ray Absorption Near-Edge Structure (XANES) Spectroscopy. *Rev. Mineral. Geochemistry*, **78** (1), 75–138.
61. De Groot, F.M.F. (1994) X-ray absorption and dichroism of transition metals and their compounds. *J. Electron Spectros. Relat. Phenomena*, **67** (4), 529–622.

62. Smith, J.W., and Saykally, R.J. (2017) Soft X-ray Absorption Spectroscopy of Liquids and Solutions. *Chem. Rev.*, **117** (23), 13909–13934.
63. Ament, L.J.P., Van Veenendaal, M., Devereaux, T.P., Hill, J.P., and Van Den Brink, J. (2011) Resonant inelastic x-ray scattering studies of elementary excitations. *Rev. Mod. Phys.*, **83** (2), 705–767.
64. Månsson, M., and Sugiyama, J. (2013) Muon-spin relaxation study on Li- and Na-diffusion in solids. *Phys. Scr.*, **88** (6), 068509.
65. Blundell, S.J. (1999) Spin-polarized muons in condensed matter physics. *Contemp. Phys.*, **40** (3), 175–192.
66. Reid, I.D., and Roduner, E. (2016) *Muon spin resonance spectroscopy, applications*, Elsevier Ltd.
67. Ikedo, Y., Sugiyama, J., Ofer, O., Månsson, M., Sakurai, H., Takayama-Muromachi, E., Ansaldo, E.J., Brewer, J.H., and Chow, K.H. (2010) Comparative μ +SR study of the zigzag chain compounds NaMn₂O₄ & LiMn₂O₄. *J. Phys. Conf. Ser.*, **225**, 012017.
68. Sugiyama, J., Nozaki, H., Månsson, M., Pra, K., Andreica, D., Amato, A., Isobe, M., and Ueda, Y. (2012) μ +SR study on ferromagnetic hollandite K₂Cr₈O₁₆ and Rb₂Cr₈O₁₆. *Phys. Rev. B - Condens. Matter Mater. Phys.*, **85**, 214407.
69. Ofer, O., Ikedo, Y., Goko, T., Månsson, M., Sugiyama, J., Ansaldo, E.J., Brewer, J.H., Chow, K.H., and Sakurai, H. (2010) Magnetic structure of the zigzag chain family Na_xCa_{1-x}V₂O₄ determined by muon-spin rotation. *Phys. Rev. B - Condens. Matter Mater. Phys.*, **82**, 094410.
70. Nozaki, H., Sugiyama, J., Månsson, M., Harada, M., Pomjakushin, V., Sikolenko, V., Cervellino, A., Roessli, B., and Sakurai, H. (2010) Incommensurate spin-density-wave order in quasi-one-dimensional metallic antiferromagnet NaV₂O₄. *Phys. Rev. B - Condens. Matter Mater. Phys.*, **81**, 100410.
71. Forslund, O.K., Papadopoulos, K., Nocerino, E., Morris, G., Hitti, B., Arseneau, D., Pomjakushin, V., Matsubara, N., Orain, J.C., Svedlindh, P., Andreica, D., Jana, S., Sugiyama, J., Månsson, M., and Sassa, Y. (2020) Intertwined magnetic sublattices in the double perovskite compound LaSrNiReO₆. *Phys. Rev. B*, **102** (14), 144409.
72. Sugiyama, J., Ikedo, Y., Månsson, M., Brewer, J.H., Stubbs, S.L., Ansaldo, E.J., Chow, K.H., Lord, J.S., Ohta, H., Michioka, C., and Yoshimura, K. (2010) Magnetic and superconducting nature of Na_{0.35}CoO₂·yH₂O and Na_{0.35}CoO₂·yD₂O investigated by muon-spin spectroscopy. *Phys. Rev. B - Condens. Matter Mater. Phys.*, **82**, 214505.
73. Uemura, Y.J., Luke, G.M., Sternlieb, B.J., Brewer, J.H., Carolan, J.F., Hardy, W.N., Kadono, R., Kempton, J.R., Kiefl, R.F., Kretzman, S.R., Mulhern, P., Riseman, T.M., Williams, D.L., Yang, B.X., Uchida, S., Takagi, H., Gopalakrishnan, J., Sleight, A.W., Subramanian, M.A., Chien, C.L., Cieplak, M.Z., Xiao, G., Lee, V.Y., Statt, B.W., Stronach, C.E., Kossler, W.J., and Yu, X.H. (1989) Universal correlations between T_c and nsm* (Carrier density over effective mass) in High-T_c cuprate superconductors. *Phys. Rev. Lett.*, **62** (19), 2317–2320.
74. Sugiyama, J., Nozaki, H., Harada, M., Kamazawa, K., Ikedo, Y., Miyake, Y., Ofer, O., Månsson, M., Ansaldo, E.J., Chow, K.H., Kobayashi, G., and Kanno, R. (2012) Diffusive behavior in LiMPO₄ with M=Fe, Co, Ni probed by muon-spin relaxation. *Phys. Rev. B - Condens. Matter Mater. Phys.*, **85**, 054111.

75. Matsubara, N., Nocerino, E., Forslund, O.K., Zubayer, A., Papadopoulos, K., Andreica, D., Sugiyama, J., Palm, R., Guguchia, Z., Cottrell, S.P., Kamiyama, T., Saito, T., Kalaboukhov, A., Sassa, Y., Masese, T., and Månsson, M. (2020) Magnetism and ion diffusion in honeycomb layered oxide $K_2Ni_2TeO_6$. *Sci. Rep.*, **10**, 18305.
76. Benedek, P., Forslund, O.K., Nocerino, E., Yazdani, N., Matsubara, N., Sassa, Y., Jurányi, F., Medarde, M., Telling, M., Månsson, M., and Wood, V. (2020) Quantifying Diffusion through Interfaces of Lithium-Ion Battery Active Materials. *ACS Appl. Mater. Interfaces*, **12** (14), 16243–16249.
77. Umegaki, I., Kawauchi, S., Sawada, H., Nozaki, H., Higuchi, Y., Miwa, K., Kondo, Y., Månsson, M., Telling, M., Coomer, F.C., Cottrell, S.P., Sasaki, T., Kobayashi, T., and Sugiyama, J. (2017) Li-ion diffusion in Li intercalated graphite C6Li and C12Li probed by μ +SR. *Phys. Chem. Chem. Phys.*, **19** (29), 19058–19066.
78. Umegaki, I., Higuchi, Y., Nozaki, H., Kondo, Y., Oka, H., Makimura, Y., Forslund, O.K., Månsson, M., Cottrell, S.P., and Sugiyama, J. (2019) Battery Materials Research with Muon Beam. *JPS Conf. Proc.*, **25**, 011009.
79. Sugiyama, J., Nozaki, H., Umegaki, I., Mukai, K., Miwa, K., Shiraki, S., Hitosugi, T., Suter, A., Prokscha, T., Salman, Z., Lord, J.S., and Månsson, M. (2015) Li-ion diffusion in $Li_4Ti_5O_{12}$ and $LiTi_2O_4$ battery materials detected by muon spin spectroscopy. *Phys. Rev. B - Condens. Matter Mater. Phys.*, **92**, 014417.
80. Månsson, M., Umegaki, I., Nozaki, H., Higuchi, Y., Kawasaki, I., Watanabe, I., Sakurai, H., and Sugiyama, J. (2014) Na-ion dynamics in Quasi-1D compound NaV_2O_4 . *J. Phys. Conf. Ser.*, **551**, 012035.
81. Arrhenius, S. (1889) Über die Reaktionsgeschwindigkeit bei der Inversion von Rohrzucker durch Säuren. *Zeitschrift für Phys. Chemie*, **4U** (1), 226–248.
82. Laidler, K.J. (1984) The development of the arrhenius equation. *J. Chem. Educ.*, **61** (6), 494–498.
83. Schafzahl, L., Hanzu, I., Wilkening, M., and Freunberger, S.A. (2017) An Electrolyte for Reversible Cycling of Sodium Metal and Intercalation Compounds. *ChemSusChem*, **10** (2), 401–408.
84. Lindgren, F., Rehlund, D., Pan, R., Pettersson, J., Younesi, R., Xu, C., Gustafsson, T., Edström, K., and Nyholm, L. (2019) On the Capacity Losses Seen for Optimized Nano-Si Composite Electrodes in Li-Metal Half-Cells. *Adv. Energy Mater.*, **9** (33).
85. Palanisamy, M., Kim, H.W., Heo, S., Lee, E., and Kim, Y. (2017) Insights into the Dual-Electrode Characteristics of Layered $Na_{0.5}Ni_{0.25}Mn_{0.75}O_2$ Materials for Sodium-Ion Batteries. *ACS Appl. Mater. Interfaces*, **9** (12), 10618–10625.
86. Buchholz, D., Moretti, A., Kloepsch, R., Nowak, S., Siozios, V., Winter, M., and Passerini, S. (2013) Toward na-ion batteries - Synthesis and characterization of a novel high capacity na ion intercalation material. *Chem. Mater.*, **25** (2), 142–148.
87. Hasa, I., Buchholz, D., Passerini, S., and Hassoun, J. (2015) A Comparative Study of Layered Transition Metal Oxide Cathodes for Application in Sodium-Ion Battery. *ACS Appl. Mater. Interfaces*, **7** (9), 5206–5212.
88. Liu, Y.-S., Pickup, D.M., Chadwick, A. V., Roberts, M.R., Bruce, P.G., Edström, K., Hao, R., Guerrini, N., Duda, L.C., Luo, K., and Guo, J. (2016) Charge-compensation in 3d-transition-metal-oxide intercalation cathodes through the generation of localized electron holes on oxygen. *Nat. Chem.*, **8** (7), 684–691.

89. Gent, W.E., Lim, K., Liang, Y., Li, Q., Barnes, T., Ahn, S., Stone, K.H., McIntire, M., Hong, J., Song, J.H., Li, Y., Mehta, A., Ermon, S., Tyliczszak, T., Kilcoyne, D., Vine, D., Park, J., Doo, S., Toney, M.F., Yang, W., Prendergast, D., and Chueh, W.C. lithium-rich layered oxides. *Nat. Commun.*
90. Xu, J., Sun, M., Qiao, R., Renfrew, S.E., Ma, L., Wu, T., Hwang, S., Nordlund, D., Su, D., Amine, K., Lu, J., McCloskey, B.D., Yang, W., and Tong, W. (2018) Elucidating anionic oxygen activity in lithium-rich layered oxides. *Nat. Commun.*, **9** (1), 1–10.
91. Okubo, M., and Yamada, A. (2017) Molecular Orbital Principles of Oxygen-Redox Battery Electrodes. *ACS Appl. Mater. Interfaces*, **9** (42), 36463–36472.

Acta Universitatis Upsaliensis

*Digital Comprehensive Summaries of Uppsala Dissertations
from the Faculty of Science and Technology 2056*

Editor: The Dean of the Faculty of Science and Technology

A doctoral dissertation from the Faculty of Science and Technology, Uppsala University, is usually a summary of a number of papers. A few copies of the complete dissertation are kept at major Swedish research libraries, while the summary alone is distributed internationally through the series Digital Comprehensive Summaries of Uppsala Dissertations from the Faculty of Science and Technology. (Prior to January, 2005, the series was published under the title “Comprehensive Summaries of Uppsala Dissertations from the Faculty of Science and Technology”.)

Distribution: publications.uu.se
urn:nbn:se:uu:diva-449511



ACTA
UNIVERSITATIS
UPSALIENSIS
UPPSALA
2021